RESEARCH ARTICLE SUMMARY

CARDIOLOGY

Mechanical load inhibits cancer growth in mouse and human hearts

Giulio Ciucci†*, Daniela Lorizio†, Francesco S. Loffredo†, Serena Zacchigna†* *et al.*

Full article and list of author affiliations: https://doi.org/10.1126/science.ads9412

INTRODUCTION: The heart is rarely affected by cancer; both primary cardiac tumors and metastases are uncommon despite the high vascularization of the myocardium. The mechanisms underlying this resistance remain unclear.

RATIONALE: Mechanical load has been proposed as a major mechanism halting cardiomyocyte proliferation early after birth, thus limiting the regenerative potential of the adult mammalian heart. We hypothesized that it could similarly hamper the proliferation of cancer cells in the heart.

RESULTS: We first used an in vivo genetic model of cancer in mice, in which Cre-mediated recombination results in the overexpression of mutated K-Ras and deletion of p53, to confirm that the heart resists oncogenic events. Despite a comparable extent of recombination in liver, heart, and skeletal muscle, multiple cancers arose at different anatomical sites but never in the heart. In addition, we set up a mouse model of heterotopic heart transplantation to mechanically unload the heart in vivo. In this model, the aorta and pulmonary artery of the transplanted heart are surgically connected with the carotid artery and external jugular vein of the recipient animal, respectively, thereby restoring perfusion in the absence of mechanical load within the left ventricle. In parallel, we used engineered heart tissues in which mechanical load can be controlled at will. In these models, mechanical load inhibited, whereas tissue unloading promoted the proliferation of lung adenocarcinoma, colon carcinoma, and melanoma cells within the myocardium. To investigate the mechanisms underlying these effects, we used spatial transcriptomics to analyze samples of human cancers that gave rise to both cardiac and extracardiac metastases. We found that cardiac metastases shared a common transcriptional profile, independent from the origin of the primary tumor. Among the most up-regulated genes in cardiac metastases were histone demethylases. Consistently, cardiac metastases showed reduced histone 3 lysine 9 trimethylation and reduced chromatin compaction. Similar findings were observed in our experimental models of cardiac load modulation in which chromatin accessibility and histone methylation were altered at sites controlling cancer cell proliferation, as determined by single-nuclei assay for transposase-accessible chromatin with sequencing and chromatin immunoprecipitation sequencing. Nesprin-2, a protein known to mediate mechanotransduction from the cytoplasm to the nucleus, emerged as a key molecule sensing mechanical forces operating in beating hearts and translating them into reduced cell proliferation. Silencing of Nesprin-2 in lung cancer cells prior to their implantation in the heart in vivo restored the capacity of the cells to proliferate in the presence of physiological mechanical load, resulting in the formation of large tumors.

CONCLUSION: Collectively, these results shed light on the role of mechanical forces in protecting the heart from cancer and may pave the way to cancer therapies based on mechanical stimulation. □

*Corresponding author. Email: giulio.ciucci@icgeb.org (G.C.); zacchign@icgeb.org (S.Z.)
†These authors contributed equally to this work. **Cite this article as G. Ciucci *et al.*, *Science* 392, eads9412 (2026). DOI: 10.1126/science.ads9412**

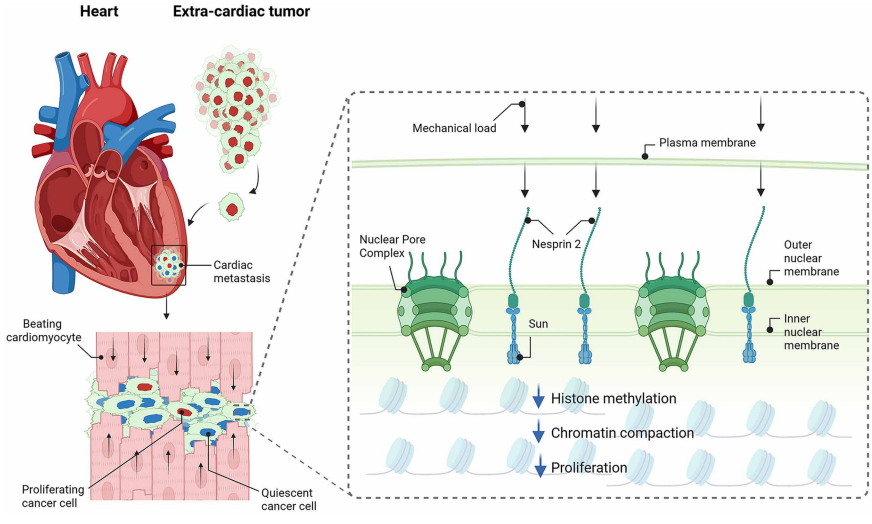

Key mechanisms inhibiting cancer cell proliferation in the heart. Cancer cells that engraft into the myocardium are exposed to mechanical forces generated by both cardiomyocyte contraction and pressure-volume load. Nesprin-2 is a key molecule in sensing these forces, resulting in reduced histone methylation and chromatin compaction in cancer cells, overall halting their proliferation. [Figure created with BioRender.com]

CARDIOLOGY

Mechanical load inhibits cancer growth in mouse and human hearts

Giulio Ciucci[1]†*, Daniela Lorizio[2]†, Nicoletta Bartoloni[1,3], Mauricio Budini[1], Andrea Colliva[1], Simone Vodret[1], Anh-Vu Nguyen[4], Lorenzo Ciacci[5], Bernhard Texler[4], Benno Cardini[4], Rupert Oberhuber[4], Sofia Bindelli[1], Ilaria Luciana Carlotta Del Giudice[1,3], Roman Vuerich[1], Francesco Riccitelli[1,3], Elena Zago[1], Henrik Nicolay Finsberg[7], Mattia Chiesa[2], Gianluca Lorenzo Perrucci[2], Rossana Bussani[3], Furio Silvestri[3], Manuel Maglione[4], Gaetano Ivan Dellino[5,6], Gianfranco Sinagra[3], Mauro Giacca[3,8], Thomas Eschenhagen[9,10], Paolo Golino[11], Giulio Pompilio[2,12], Pier Giuseppe Pelicci[5,6], Laura Andolfi[13], Maurizio Pinamonti[14], Matteo Dal Ferro[14], Samuel Wall[7], Francesco S. Loffredo[11]†, Serena Zacchigna[1,3]†*

The heart rarely develops cancer, and, at the same time, it lacks regenerative capacity, as cardiomyocytes stop proliferating after birth. This suggests that mechanisms limiting cardiac regeneration may also protect against cancer. In this work, we investigated the role of mechanical load and used in vivo cancer models and ex vivo engineered heart tissues to show that mechanical load reduces cancer cell proliferation in the myocardium. Spatial transcriptomics of human cardiac metastases revealed decreased histone methylation and chromatin compaction. These changes affect chromatin accessibility at proliferation-related loci, with Nesprin-2 identified as a key mechanosensor. Our results uncover how mechanical forces protect the heart from cancer and suggest potential strategies for cancer therapy based on mechanical stimulation.

The heart is rarely affected by cancer. Both primary cardiac tumors and metastases are rare, an enigmatic circumstance considering the high vascularization of the myocardium and the constant blood flow through cardiac chambers (*1*–*5*). The mechanisms that protect the heart from cancer remain elusive. At the same time, the adult mammalian heart exhibits poor regenerative potential, as cardiac cells stop dividing early after birth (*6*–*8*). This suggests that the same mechanisms that halt the proliferation of cardiac cells could also inhibit the growth of cancer cells in the adult heart.

Among the mechanisms that have been claimed to be responsible for the loss of cardiomyocyte (CM) proliferative potential at birth is a sudden increase in mechanical load (*7*, *9*, *10*). Consistently, cardiac unloading, as happens in end-stage heart failure patients implanted with a left ventricular assisted device (LVAD), induces CM proliferation (*11*).

In this work, we confirmed that the heart resists oncogenic events and investigated whether mechanical load affects the proliferation of cancer cells in the heart, thereby explaining the low incidence of cardiac cancer. We used both an in vivo model of mechanical unloading, obtained by heterotopic heart transplantation in mice, and engineered heart tissues (EHTs) to show that mechanical load inhibits, whereas tissue unloading promotes, cancer cell proliferation within the myocardium. We also interrogated human samples of cardiac metastases and extracardiac lesions from the same patients, combined with single-nuclei assay for transposase-accessible chromatin with sequencing (ATAC-seq) and chromatin immunoprecipitation sequencing (ChIP-seq) on cancer cells harvested from loaded and unloaded hearts in vivo, to investigate the mechanisms that inhibit cancer cell growth in the heart.

Results

Mechanical loading in the heart inhibits cancer growth in vivo

In addition to being rare, cardiac metastases tend to be smaller than extracardiac lesions, particularly for blood-borne metastases within the myocardium (*12*). This is often evident in the case of patients with highly aggressive cancers that disseminate to both the myocardium and other organs, as exemplified by the case of a patient affected by an aggressive uveal melanoma, which massively invaded both the liver and the lung and minimally affected the heart, with a few metastatic spots located mainly in the pericardial fat and very rarely within the myocardium, shown in Fig. 1A. To experimentally investigate whether the heart is protected from cancer, we systemically injected an adeno-associated virus 9 (AAV9)–based vector expressing the Cre recombinase in seven *LSL-K-Ras*$^{G12D/+}$*;p53*$^{f/f}$ mice to induce K-Ras and p53 oncogenic events in AAV target cells (Fig. 1B). Despite a comparable extent of recombination in multiple tissues (fig. S1, A to D), expression of mutated K-Ras and loss of p53 resulted in the formation of five cancers at different anatomical sites in four mice but never in the heart (Fig. 1C). The presence of healthy skeletal muscle fibers close to the tumor mass and the expression of desmin (fig. S1E) were compatible with the formation of rhabdomyosarcomas, originating from striated muscles in limbs, flank, neck, and face, in line with the high tropism of AAV vectors for skeletal muscle (*13*).

To assess the contribution of mechanical load to the low incidence and growth of cancer in the heart, we used a model of in vivo cardiac unloading by heterotopically transplanting a donor heart into the neck of a recipient syngeneic mouse. In this model, schematically represented in Fig. 1D, the aorta and pulmonary artery of the transplanted heart are surgically connected with the carotid artery and external jugular vein of the recipient animal, respectively, thereby restoring perfusion in the absence of mechanical load within the left ventricle (LV) (*14*, *15*). Echocardiography of both native (loaded) and unloaded LVs confirmed a marked reduction in all parameters of myocardial strain metrics, including velocity, displacement, longitudinal strain, and strain rate, in unloaded hearts (fig. S2, A to D, and movies S1 and S2). We observed an increased number of EdU$^+$, Ki67$^+$, and phosphohistone H3$^+$ (pHH3$^+$) CMs after 1 month of mechanical unloading in vivo together with a few CMs in which Aurora kinase B (AURKB) was localized at midbodies (fig. S2, E to L), consistent with previous evidence of regenerating CMs in human hearts, unloaded by LVAD implantation (*11*).

Leveraging this heterotopic heart transplantation (HHT) model, we injected 1×10^5 lung adenocarcinoma LG1233 cancer cells (*16*) stably expressing green fluorescent protein (GFP) intramyocardially into the LV of both loaded and unloaded hearts. We initially focused on lung cancer, as it is one of the cancer types that disseminates to the heart at a relatively high frequency, preferentially to the outer cardiac layers (epicardium and pericardium) (*3*). Cancer cells grew very poorly in native hearts exposed to physiological load, as previously described (*8*), rarely occupying more than 20% of the LV area at 2 weeks after injection (Fig. 1, E and F). By contrast, they massively proliferated and infiltrated unloaded hearts, resulting in

[1]Cardiovascular Biology Laboratory, International Centre for Genetic Engineering and Biotechnology (ICGEB), Trieste, Italy. [2]Centro Cardiologico Monzino-IRCCS, Milan, Italy. [3]Department of Medicine, Surgery and Health Sciences, University of Trieste, Trieste, Italy. [4]Daniel Swarovski Research Laboratory (DSL), Department of Visceral, Transplant and Thoracic Surgery, Centre of Operative Medicine, Medical University of Innsbruck, Innsbruck, Austria. [5]Department of Experimental Oncology, IEO, European Institute of Oncology IRCCS, Milan, Italy. [6]Department of Oncology and Hemato-Oncology, University of Milan, Milan, Italy. [7]Simula Research Laboratory, Oslo, Norway. [8]School of Cardiovascular and Metabolic Medicine & Sciences and British Heart Foundation Centre of Research Excellence, King's College London, London, UK. [9]University Medical Center Hamburg-Eppendorf, Hamburg, Germany. [10]DZHK (German Centre for Cardiovascular Research), Partner Site North, Hamburg, Germany. [11]Department of Translational Medical Sciences, Division of Cardiology, University of Campania "Luigi Vanvitelli," Naples, Italy. [12]Department of Biomedical, Surgical and Dental Sciences, University of Milano, Milano, Italy. [13]Istituto Officina dei Materiali - Consiglio Nazionale delle Ricerche, Trieste, Italy. [14]Azienda Sanitaria Integrata Giuliano Isontina (ASUGI), Trieste, Italy. ***Corresponding author. Email: giulio.ciucci@icgeb.org (G.C.); zacchigna@icgeb.org (S.Z.)** †These authors contributed equally to this work.

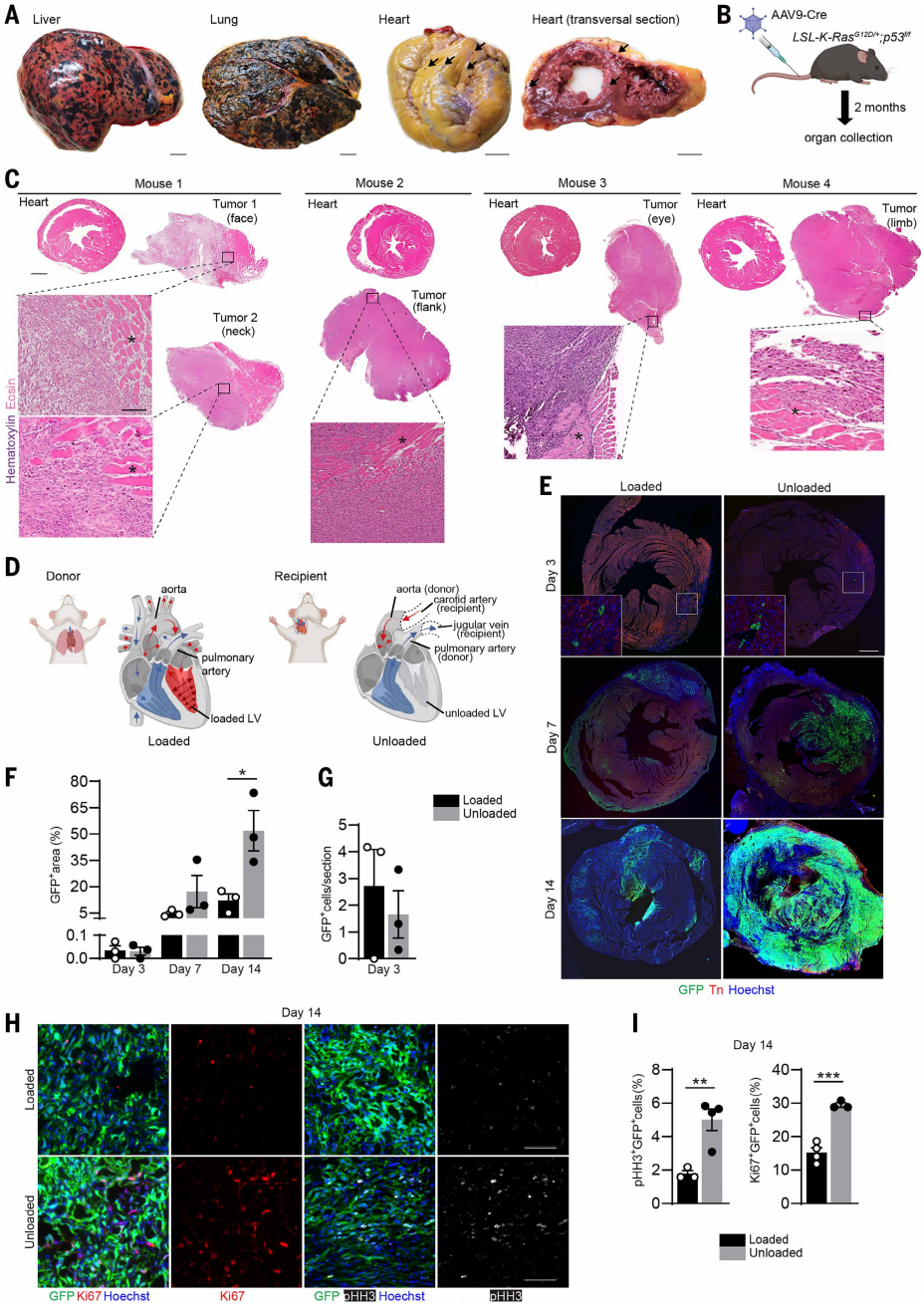

Fig. 1. Mechanical load controls cancer cell proliferation in the heart. (**A**) Gross appearance of en bloc resection of liver, lung, and heart from a patient affected by a metastatic uveal melanoma. Black arrows indicate small metastatic spots in the pericardial fat and in the myocardium. (**B**) Schematic representation of in vivo tumorigenesis experiment: AAV9-Cre vectors were injected intravenously in seven *LSL-K-Ras*$^{G12D/+}$;*p53*$^{f/f}$ mice; hearts, skeletal muscles, and livers were collected after 2 months. (**C**) Whole-organ sections of hearts and tumors from *LSL-K-Ras*$^{G12D/+}$;*p53*$^{f/f}$ mice injected with AAV9-Cre; healthy skeletal muscle fibers in high-magnification images are indicated by asterisks. (**D**) Schematic representation of the circulation following heterotopic heart transplantation. The heart is removed from the thorax of a donor mouse (left) and anastomosed to the neck vessels of a recipient mouse (right). In the transplanted heart, the oxygenated blood from the carotid artery bumps into the closed aortic valve and enters the coronary tree. The venous blood is drained back through the pulmonary artery into the jugular vein in the absence of blood flow into the LV. (**E**) Transversal sections of loaded and unloaded hearts injected with LG1233 GFP$^+$ cancer cells at the indicated time points. CMs were stained for troponin (Tn). Insets show high-magnification images of engrafted cells at day 3. (**F**) Quantification of the area occupied by GFP$^+$ cancer cells in loaded and unloaded hearts at the indicated time points ($n = 3$ biological replicates). (**G**) Quantification of GFP$^+$ cancer cells in loaded and unloaded hearts at day 3 ($n = 3$ biological replicates). (**H**) Representative images of loaded and unloaded hearts stained for the proliferation markers pHH3 and Ki67 together with GFP at day 14. (**I**) Quantification of pHH3$^+$ and Ki67$^+$ cancer cells in loaded and unloaded hearts at day 14 ($n = 3$ to 4 biological replicates). Scale bars: 1 cm (A); 1 mm [(C) (whole organ sections) and (E)]; 100 μm [(C) (high magnification insets)]; 50 μm (H). Results were analyzed by either two-way ANOVA followed by a Tukey post hoc test (F) or a two-tailed *t* test [(G) and (I)]. $^*P < 0.05$; $^{**}P < 0.01$; $^{***}P < 0.001$. Data are mean ± SD.

extensive CM death and replacement (fig. S3) and almost complete disappearance of healthy myocardium at 2 weeks (Fig. 1, E and F). The increased growth of cancer cells in unloaded hearts was not due to a higher engraftment, as the number of GFP$^+$ cells at day 3 was comparable in control (loaded) and unloaded hearts (Fig. 1, E and G). We also analyzed cell death by both TUNEL and staining for cleaved Caspase 3 (cCASP3) to detect cancer cell apoptosis and staining for RIP3 to detect necrosis. We did not find any GFP$^+$TUNEL$^+$, GFP$^+$cCASP3$^+$, or GFP$^+$RIP3$^+$ cells in either control or unloaded hearts at day 3 after injection (fig. S4, A to C), thus excluding the possibility that the different tumor size at day 14 was due to a higher rate of cell death in control hearts.

Next, we analyzed cell proliferation by quantifying the number of cells positive for Ki67 and pHH3, which label all active phases of the cell cycle and mitosis or late G2, respectively. Both markers indicated a twofold increase in the number of proliferating cancer cells in unloaded hearts at both day 7 (fig. S4, D and E) and 14 after cell injection (Fig. 1, H and I).

Collectively, these data indicate that lung cancer cells form larger tumors in unloaded hearts than in control (loaded) hearts and that this is due to increased cell proliferation in unloaded conditions.

Mechanical load inhibits cancer cell proliferation in engineered cardiac tissues

To confirm the effect of mechanical load in a simpler model, we adapted the EHT system (*17*), composed of neonatal rat CMs and fibroblasts, by inserting two metal braces to tune mechanical load at will (Fig. 2A). Specifically, braces can be rotated to either increase stiffness of the silicone posts the tissue is anchored to (increased load) or reduce the distance between the two tissue extremities, thereby resulting in unloading (Fig. 2A).

To evaluate the robustness of EHTs to study the effect of load variation on cell proliferation, we first looked at CMs. As expected, mechanical unload increased CM proliferation at day 3, assessed by EdU incorporation, staining for the proliferation markers Ki67 and pHH3, and quantification of CM density (fig. S5, A to G), in line with the results obtained in vivo in heterotopically transplanted hearts. By contrast, prolonged loading for 2 weeks reduced CM proliferation, as assessed by staining for both Ki67 and pHH3 (fig. S5, H and I). EdU$^+$ nuclei were minimally increased in conditions of increased load (fig. S5J), mostly incorporated into binucleated CMs (fig. S5, K and L), consistent

with improved CM maturation. The positive effect of mechanical load on CM maturation was confirmed by their increased cross-sectional area and force of contraction (fig. S5, M to P). Thus, mechanical unload promotes CM proliferation, whereas the opposite happens by increasing the load, which reduces proliferation and induces CM maturation.

Next, we generated EHTs with the inclusion of GFP^+ lung cancer cells (Fig. 2B). After 7 days, a time sufficient for CM maturation and appearance of coherent beating, we rotated the metal braces to either decrease or increase mechanical load for an additional 3 days. Similar to what was observed for CMs, unloading promoted the proliferation of cancer cells within the EHTs, whereas overloading halted it (Fig. 2, C and D). These data are consistent with the effect of in vivo unloading by HHT on cancer cell proliferation (Fig. 1).

To verify to what extent the EHT system reproduces the major types of mechanical forces that operate in a beating heart, we ran mathematical simulations on cardiac mechanics. Figure S6A shows an idealized rodent LV in which myofiber distribution rotates transmurally from the endocardium (red, +60°) to the epicardium (blue, −60°). This LV contracts against a standard systolic cavity pressure or, in the unloaded setup, against no pressure (fig. S6B). This has a dramatic effect on the calculated stresses along the myofiber orientation (σ_{ff}), the aligned sheet direction (σ_{ss}), and the direction normal to these (σ_{nn}), reducing their magnitudes substantially in all the three major components (fig. S6C). These models were validated using real echocardiography measurements in loaded and unloaded hearts (fig. S6, D and E) and agreed with strain parameters shown in fig. S2.

Next, we built a model for the EHT, assuming that it has a cylindrical shape and contracts against a spring constant that approximates the contraction, experimentally measured at peak systole (~15% of the EHT length), as shown in fig. S6F. Mechanical stresses were then calculated for the three configurations shown in Fig. 2A, namely during standard beating (control), unloading, and increased load. As shown in fig. S6G, the EHT exhibited the same stress patterns as the LV simulation in the fiber stress (σ_{ff}) and orthogonal normal stresses, both circumferential (σ_c) and radial (σ_r). Increased load resulted in a substantial increase in magnitude of all stress components, whereas any stress effectively disappeared in unloaded conditions.

Collectively, these data indicate that load modulation in EHTs reproduces the effect of cardiac unloading in vivo and that modulation of mechanical load has comparable effects on the proliferation of cardiac and cancer cells both in vivo and in EHTs.

Cancer cells preferentially grow in EHT regions exposed to low mechanical pressure

The EHT unloading system described in Fig. 2A is not compatible with long-term experiments, as the unloaded tissue extensively remodels and tends to lose its original three-dimensional (3D) structure over time. Therefore, we used an alternative model in which CM contractility was modulated by the availability of calcium in the medium to assess the effect of prolonged cardiac unloading on cancer cell growth. We incorporated GFP^+ lung cancer cells in tissues cultured either in the absence or in the presence of calcium, which resulted in static and beating EHTs, respectively (Fig. 2E). In line with our previous data, GFP^+ cancer cells grew more and occupied a larger area in static than in beating EHTs, as shown and quantified for whole EHTs in Fig. 2, E and F, and for the corresponding cross-sections in Fig. 2, G and H. This was paralleled by reduced cell proliferation in beating EHTs (Fig. 2, I and J). As shown in fig. S7, the absence of calcium did not influence LG1233 cell proliferation in pure 2D cultures.

We also observed that cancer cells localized preferentially in the outer layers of beating EHTs, avoiding the central part, whereas they were evenly distributed in static EHTs (Fig. 2G). By leveraging our simulated EHT model, shown in fig. S6F, we characterized the beating EHT along the radial direction over an entire simulated twitch, taking into account the higher number of myocytes toward the outer layers of the EHT, as observed microscopically. The results of this analysis in fig. S8, A and B, showed higher hydrostatic pressure in the internal region of the EHT at peak systole. By quantifying the number of cancer cells in multiple concentric layers within each EHT, we confirmed that they were equally distributed in static EHTs. By contrast, in beating EHTs, cancer cell density formed a gradient that was inversely related to the one of hydrostatic pressure (fig. S8C), suggesting that higher compressive forces negatively modulated cancer cell proliferation.

The reduced proliferation of LG1233 cells in the center of beating EHTs could be due to metabolic competition for nutrients between CMs and cancer cells. To experimentally assess this hypothesis, we harvested the supernatant from both static and beating EHTs and added it to LG1233 cells. We did not observe any change in LG1233 cell proliferation, indicating that similar nutrient content was available in the two media (fig. S9, A and B). In addition, we cocultured LG1233 cells with neonatal rat CMs, either kept in physiological conditions or paced at 180 beats per minute. As shown in fig. S9, C to F, LG1233 cells proliferated less in the presence of paced CMs, but this did not result in different glucose uptake, showing that there was no major metabolic competition between CMs and cancer cells.

Thus, both mechanical load and compressive forces generated by CM contraction inhibit cancer cell proliferation in EHTs, independent of major alterations in nutrient availability.

Histone demethylases are up-regulated in human cardiac metastases

To investigate the molecular mechanisms by which cancer cells sense mechanical stimuli in the beating heart and translate them into inhibition of cell proliferation, we interrogated the transcriptional profile of cancer cells that naturally grow in the myocardium, as in the case of human cardiac metastases. We collected samples from patients affected by three different primary tumors (lung adenocarcinoma, colon carcinoma, and cutaneous melanoma), which disseminated to both the heart and other organs, depicted in Fig. 3A. On these samples, we performed spatial transcriptomics using the GeoMX technology, which allows profiling the transcriptome of specific cell types by capturing cells identified by specific markers. In particular, we stained and captured lung and colon carcinoma cells with antipancytokeratin antibodies and melanoma cells with antipremelanosome protein (PMEL) antibodies (Fig. 3B) and compared the expression profiles of cancer cells in either cardiac metastases or extracardiac sites, including both primary tumors and extracardiac metastases. Unsupervised hierarchical clustering based on the most differentially expressed genes [DEGs, $n = 1753$, analysis of variance (ANOVA) $P < 0.01$] allowed complete separation between cardiac metastases, primary tumors, and extracardiac metastases and showed that cardiac metastases shared a common transcriptional profile independent from the origin of the tumor (Fig. 3C). Gene ontology revealed that the most enriched pathway in cardiac metastases was "histone demethylation," showing the highest number of DEGs and the highest levels of gene up-regulation (Fig. 3D and table S1). When comparing multiple regions of interest (ROIs) within cardiac metastases, we found that most histone demethylases were particularly up-regulated in the center of the lesion compared with its border (fig. S10), in line with the results obtained in EHTs (fig. S8).

Consistent with the up-regulation of several histone demethylases, the levels of histone 3 lysine 9 trimethylation (H3K9me3) were lower in the nuclei of cardiac metastases compared with those detected in primary tumors and extracardiac metastases (Fig. 3, E and F). These changes in H3K9me3 were paralleled by an altered chromatin state, which was less compact in cardiac metastases than in extracardiac lesions. As shown in Fig. 3, G and H, the coefficient of variation (CV) of DNA compaction, a commonly used method to assess chromatin compaction (*18*–*20*), was reduced in cardiac metastases compared with that in extracardiac lesions.

Thus, cancer cells that reach the human heart up-regulate histone demethylases, which results in a reduction of both H3K9me3 and chromatin compaction.

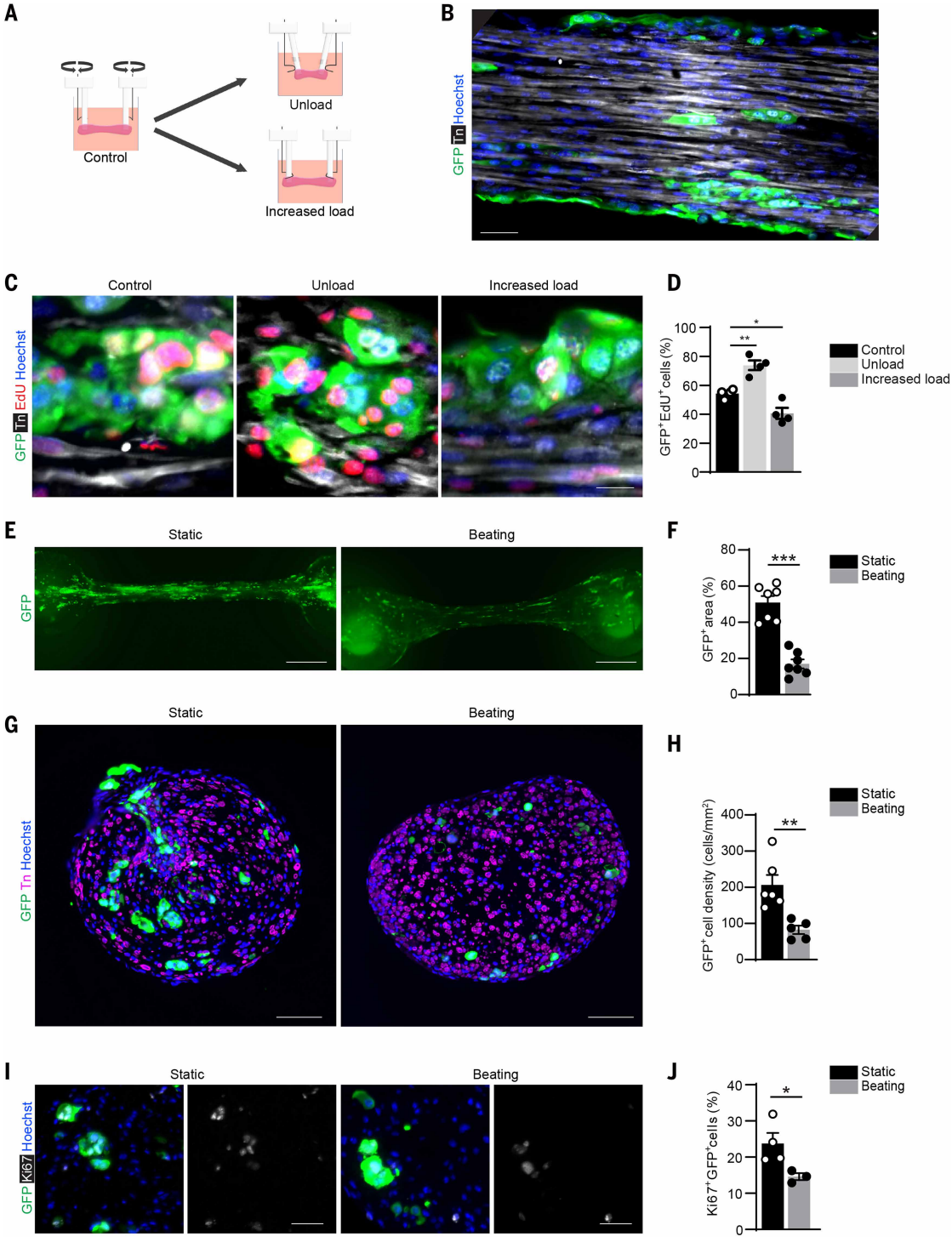

Fig. 2. Mechanical load controls cancer cell proliferation in EHT. (**A**) Schematic representation of control EHT (left) and its adaptation to induce either unloading (top right) or increased load (bottom right). (**B**) Representative immunofluorescence image of an EHT composed of both Tn^+ CMs and GFP^+ cancer cells. (**C**) Immunofluorescence images of EHTs exposed to control, unloading, and increased load stained for GFP, Tn, and EdU. (**D**) Quantification of the percentage of proliferating EdU^+ cancer cells in EHTs exposed to control, unloading, and increased load ($n = 3$ to 4 biological replicates). (**E**) Representative low-magnification images of EHTs composed of both CMs and LG1233 GFP^+ cancer cells cultured in the absence (static) or presence (beating) of calcium. (**F**) Quantification of the area occupied by LG1233 GFP^+ cancer cells in static and beating EHTs ($n = 7$ biological replicates). (**G**) Representative cross sections of static and beating EHTs stained for Tn and GFP. (**H**) Quantification of LG1233 GFP^+ cancer cell density in static and beating EHTs ($n = 5$ to 6 biological replicates). (**I**) Representative immunofluorescence staining of static and beating EHTs stained for Ki67 and GFP. (**J**) Quantification of $Ki67^+$ proliferating LG1233 GFP^+ cancer cells in static and beating EHTs ($n = 3$ to 4 biological replicates). Scale bars: 50 μm [(B) and (I)]; 20 μm (C); 1 mm (E); 100 μm (G). Results were analyzed by either one-way ANOVA followed by a Dunnett's post hoc test (D) or a two-tailed *t* test [(F), (H), and (J)]. $^*P < 0.05$; $^{**}P < 0.01$; $^{***}P < 0.001$. Data are mean ± SD.

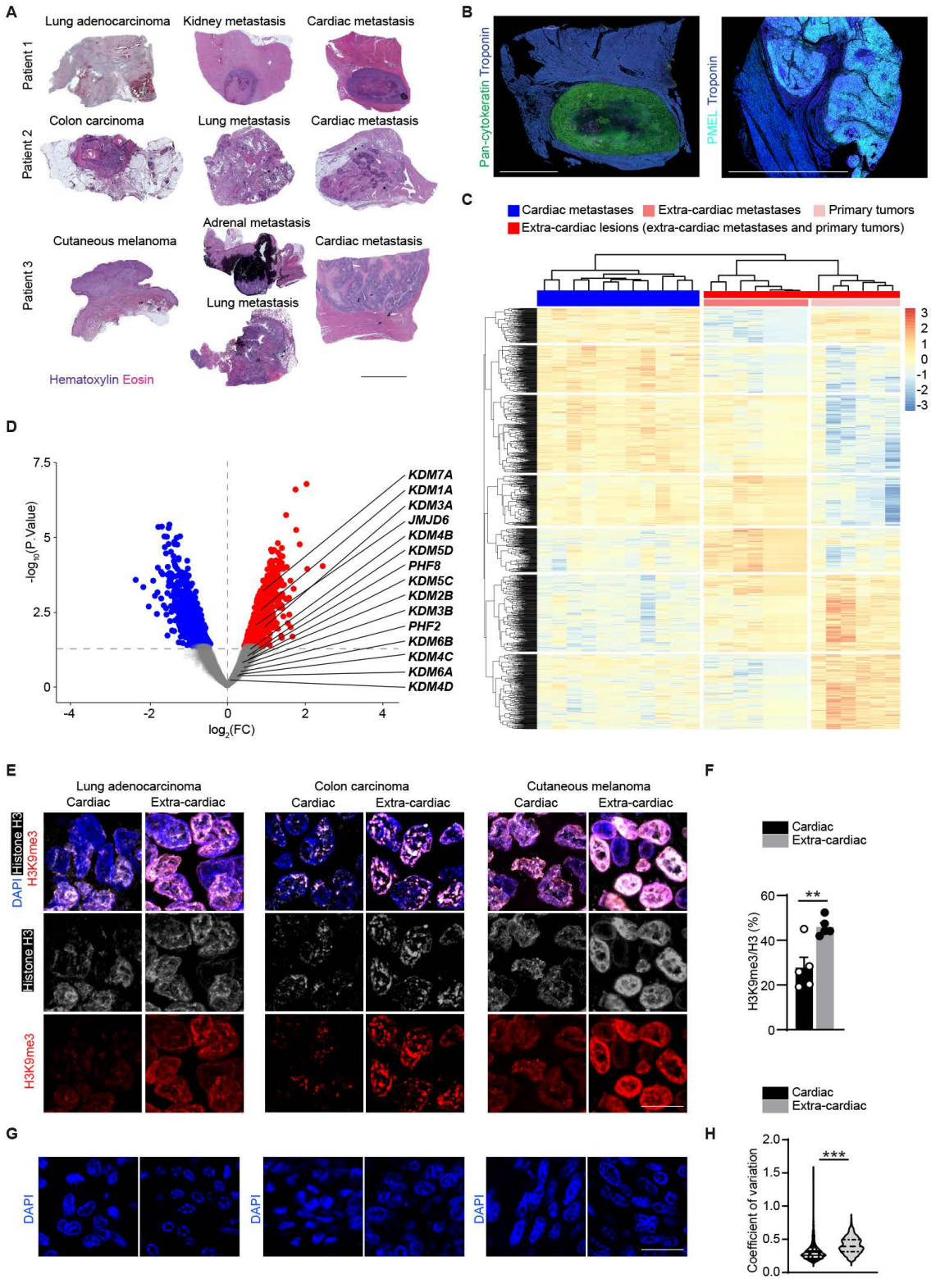

Fig. 3. Spatial transcriptomics on human samples reveals lower levels of histone methylation and chromatin compaction in cardiac metastases compared to extracardiac tumors. (**A**) Hematoxylin or eosin staining of primary cancers that disseminated to both the heart and extracardiac sites. (**B**) Representative immunofluorescence of cardiac metastases in which carcinoma cells were stained for pancytokeratin, melanoma cells were stained for PMEL, and CMs were stained for Troponin. (**C**) Heat map showing unsupervised clustering based on most differentially expressed genes. Gene expression was expressed as normalized value after row standardization and displayed as gradient colors from higher (dark red) to lower (dark blue) expression. (**D**) Volcano plot of differential gene expression comparing cardiac and extracardiac metastases, with indication of the most up-regulated genes belonging to the histone demethylation pathway in cardiac metastases. Log_2(FC) (FC, fold change) and $-log_{10}$(*P*) are represented on

the *x* axis and *y* axis, respectively. Red and blue dots denote genes significantly overexpressed or silenced in cardiac metastases, respectively ($P < 0.05$), whereas gray dots represent genes without difference in expression between the two groups. (**E**) Representative images of H3K9me3 in the nuclei of cardiac and extracardiac lesions from the samples analyzed by spatial transcriptomics. (**F**) Quantification of colocalization of H3K9me3 and H3 in cardiac and extracardiac lesions from the samples analyzed by spatial transcriptomics ($n = 14$ to 25 microscopic fields from three cardiac metastases and seven extracardiac tumors). (**G**) Representative images of chromatin compaction in the nuclei of cardiac and extracardiac lesions from the samples analyzed by spatial transcriptomics. (**H**) Coefficient of variation calculated based on the DAPI fluorescent images represented in (G) ($n = 1184$ to 2370 nuclei from three cardiac metastases and seven extracardiac tumors). Scale bars: 1 cm (A); 0.5 cm (B); 20 μm [(E) and (G)]. Results in (F) and (H) were analyzed by a two-tailed *t* test. $^{**}P < 0.01$; $^{***}P < 0.001$. Data are mean ± SD.

Mechanical load reduces histone methylation and chromatin compaction, altering accessibility in genomic regions relevant for cancer growth

To validate the effect of mechanical load on histone methylation and chromatin compaction, we analyzed the same parameters in our experimental models of load modulation. First, we stained loaded and unloaded hearts injected with LG1233 cancer cells for H3K9me3 and observed that loaded hearts showed reduced H3K9m3 (Fig. 4, A and B), which was paralleled by decreased chromatin compaction (Fig. 4, C and D). In the same model, we also performed single-nuclei ATAC-seq on cancer cells harvested from loaded and unloaded hearts to analyze chromatin accessibility within gene regulatory regions. Peak calling and analysis of differentially accessible regions (DARs) demonstrated higher chromatin accessibility in cancer cells grown in loaded hearts. Gene ontology revealed a few pathways particularly enriched in loaded hearts, including "cell cycle arrest," "extracellular sensing," "mechanosensing," "cytoskeleton," "chromosomal instability," and "calcium homeostasis," correlated with marked accessibility in regions associated with calcium-dependent (*Ccbe1*, *Syt6*) and mechanosensing genes (*Piezo2*, *Add2*) (Fig. 4, E and F). On the other hand, pathways related to "cancer cell metabolism" were selectively less active in loaded hearts (Fig. 4E).

To verify whether increased chromatin accessibility was associated with loss of the H3K9me3 heterochromatin mark, we profiled H3K9me3 genomic distribution using ChIP-seq assay. Almost all the significantly ($P < 0.05$) different H3K9me3 peaks showed a reduction of ChIP-seq signal intensity in loaded compared with in unloaded hearts (Fig. 4G). We again performed gene ontology and found that pathways identified by the analysis of DARs and differentially H3K9me trimethylated regions largely overlapped. In particular, regulatory regions of genes encoding for proteins that drive specific steps in the biological pathways activated by loading showed both increased chromatin accessibility and reduction of H3K9me3 ChIP-seq signals, including genes known to inhibit cancer cell proliferation (*Fam107b*, *Ptprs*, and *Spred2*; Fig. 4E and fig. S11A). Consistently, a good correlation was found between the *t*-statistics of genes commonly identified by ATAC-seq and ChIP-seq (correlation coefficient $r = 0.51$, $P < 0.0001$; fig. S11B). To further assess the functional link between chromatin compaction and histone methylation, we analyzed static and beating EHTs. Also in this case, mechanical load induced by cardiac beat resulted in reduced chromatin compaction and H3K9me3 (Fig. 5, A to D). To assess whether H3K9me3 was not only associated with but causally linked to cancer cell proliferation, we silenced the major lysine-specific demethylases (KDMs), which target H3K9 (*21*) and were up-regulated in human cardiac metastases. As expected, silencing of both KDM4C and KDM4D (fig. S12A) as well as their combination in LG1233 cells, prior to their inclusion in EHTs, resulted in increased H3K9me3 (Fig. 5, E and F). This increase was in turn associated with larger areas occupied by cancer cells as well as higher LG1233 cell density in beating EHTs (Fig. 5, G to J).

Thus, mechanical load reduces chromatin compaction and H3K9me, with relevant modification in chromatin accessibility in genomic regions that control cancer cell proliferation both in vivo and in EHTs.

Nesprin-2 translates mechanical load into reduced cancer cell proliferation

Next, we investigated the mechanism by which mechanical forces affect chromatin accessibility. A key mechanotransducer, which translates extracellular stimuli into nuclear responses, is the linker of nucleoskeleton and cytoskeleton (LINC) complex, composed of nesprin and sun proteins in the outer and inner membrane, respectively (*22*). To explore whether members of the LINC complex are required by cancer cells to sense mechanical load and translate it into an inhibition of cell proliferation, we individually silenced each of the four nesprins (*Syne1*, *Syne2*, *Syne3*, and *Syne4*) as well as the two sun protein coding genes (*Sun1* and *Sun2*) by specific small interfering RNAs (siRNAs) in LG1233 cells (fig. S12, A to D) and assessed their proliferation in beating EHTs. As shown in Fig. 6, A and B, silencing of both Nesprin-2 and Nesprin-4 increased the area occupied by LG1233 cells as well as LG1233 cell density in EHT cross-sections (Fig. 6, C and D), whereas none of the siRNAs promoted cell proliferation in 2D pure cell culture (fig. S13). Next, we assessed the expression and silenced both Nesprin-2 and Nesprin-4 in additional cancer cell lines, representative of the cancer types analyzed in our spatial transcriptomics on cardiac metastasis, namely CT26 colon cancer cells and B16-F10 melanoma cells (fig. S14, A to E), and again assessed their proliferation in beating EHTs. Silencing of Nesprin-2 resulted in increased area occupied by cancer cells and cell density within EHT cross-sections for both CT26 cells (fig. S14, F to H) and B16-F10 cells (fig. S14, I to K), pointing to Nesprin-2 as a key mechanotransducer in controlling the proliferation of multiple cancer cell types in beating cardiac tissues. Also in these cell lines, silencing of either Nesprin-2 or Nesprin-4 did not affect cell proliferation in culture (fig. S14, L to S). Next, we assessed whether Nesprin-2 was required to alter chromatin status in response to mechanical load. As shown in Fig. 6, E to H, silencing of Nesprin-2 in LG1233 cells increased both chromatin compaction and H3K9 methylation in beating EHTs.

To further link Nesprin-2 with cardiac mechanotransduction, we repeated the experiment in both static and overloaded EHTs. Nesprin-2 silencing in static EHTs did not affect the size of the area occupied by LG1233 (fig. S15, A and B) and B16-F10 cells (fig. S15, C and D). The increase in the area occupied by Nesprin-2-silenced CT26 cancer cells in static EHTs (fig. S15, E and F) was unlikely due to cell proliferation, as cell density was not affected (fig. S15, G and H), but was rather due to cell size increase upon Nesprin-2 silencing (fig. S14O). In all cell types, the effect of Nesprin-2 silencing was even higher in the presence of increased mechanical load (fig. S15, I and J for LG1233, K and L for CT26, and M and N for B16-F10 cells) when many cells proliferated also in the central part of the EHT, characterized by high hydrostatic compressive pressure (0 to 120 mm, fig. S15O).

Lastly, we silenced Nesprin-2 in LG1233 cells prior to their implantation in vivo in beating hearts (fig. S16). Consistent with the data obtained in EHTs, silencing of Nesprin-2 allowed cancer cells to extensively expand and proliferate within the myocardium (Fig. 6, I to L). In line with the previous results, Nesprin-2 silencing increased chromatin compaction and H3K9me3 in LG1233 cells implanted in beating hearts (Fig. 6, M to P).

Collectively, our data show that mechanical load in beating heart tissue reduces histone methylation and chromatin compaction in cancer cells, resulting in increased chromatin accessibility at sites that control cancer cell proliferation. Nesprin-2 is a key mediator in this mechanotransduction process that inhibits cancer cell growth in the heart.

Discussion

In this manuscript, we demonstrated that variations in mechanical load have a dramatic effect on the growth of cancer cells within heart

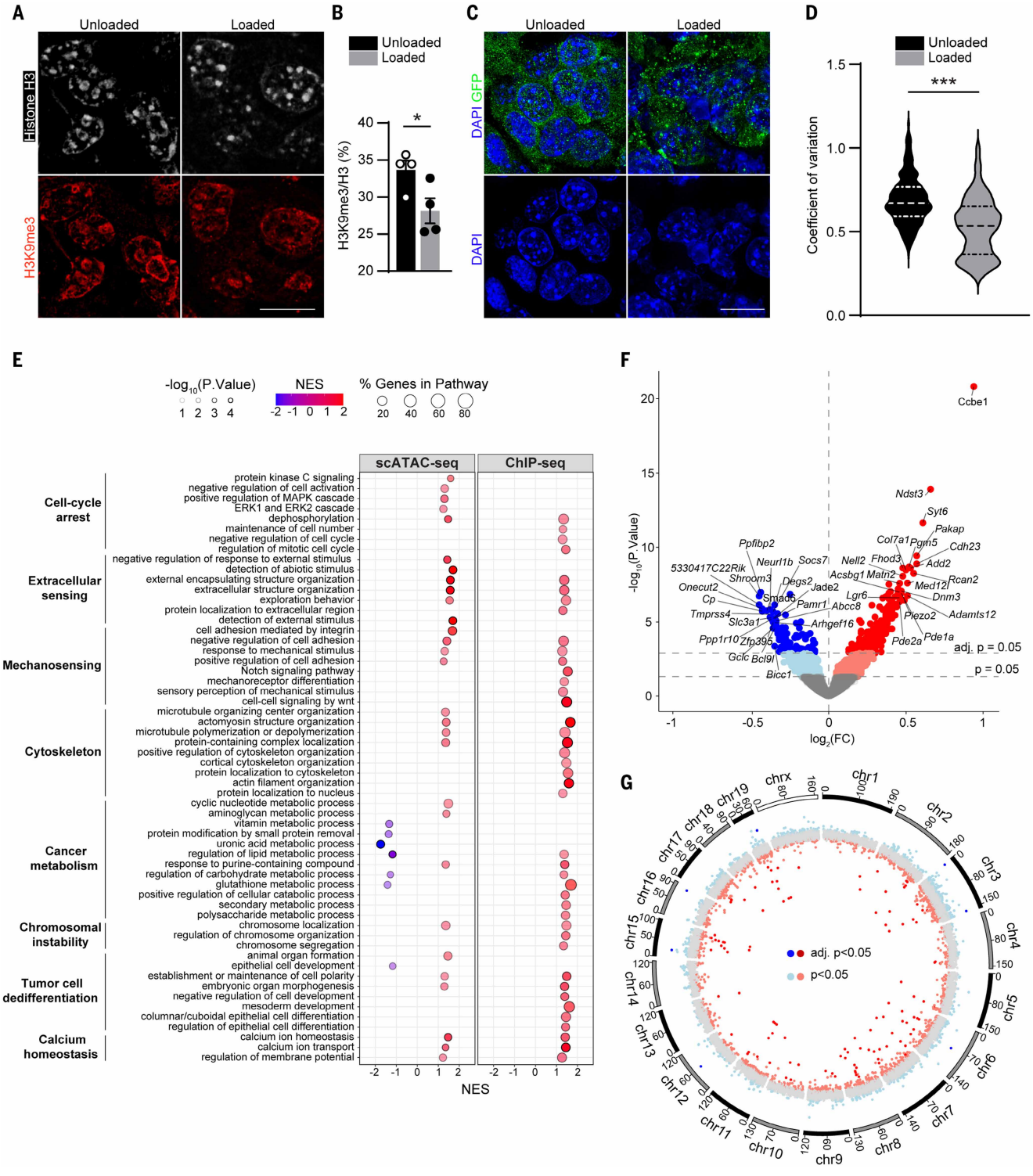

Fig. 4. Mechanical load reduces chromatin compaction and H3K9me3 in vivo associated with altered chromatin accessibility. (**A** and **B**) Representative images (A) and quantification (B) of colocalization between H3K9me3 and H3 in LG1233 GFP$^+$ cancer cells in loaded and unloaded hearts ($n = 4$ biological replicates). (**C** and **D**) Representative images (C) and quantification (D) of chromatin compaction by DAPI staining of LG1233 GFP$^+$ cancer cells in loaded and unloaded hearts ($n = 840$ to 860 nuclei from three loaded and five unloaded hearts). (**E**) Results of GSEA on DARs and H3K9me3 peaks between loaded and unloaded hearts, grouping gene sets by process. Red dots indicate a significant enrichment; blue dots incidcate a significant depletion. The dot size shows the number of DAR or H3K9me3 peaks in each gene set, and results are ordered from high to low normalized enrichment score (NES) levels. (**F**) Volcano plot showing DARs between loaded and unloaded hearts ($n = 2$ biological replicates). Blue and red indicate highly accessible peaks in unloaded and loaded samples, respectively; gray indicates no difference between samples. (**G**) Circos plot showing log2FC ChIP-seq signal intensity of H3K9me3 peaks in loaded versus unloaded samples; red and blue dots indicate peaks showing significantly reduced and increased signals, respectively. Gray segments in the outer circle represent the 20 chromosomes of the mouse genome. Scale bars: 20 μm (A); 10 μm (C). Results in (B) and (D) were analyzed by a two-tailed *t* test. $^*P < 0.05$; $^{***}P < 0.001$. Data are mean ± SD.

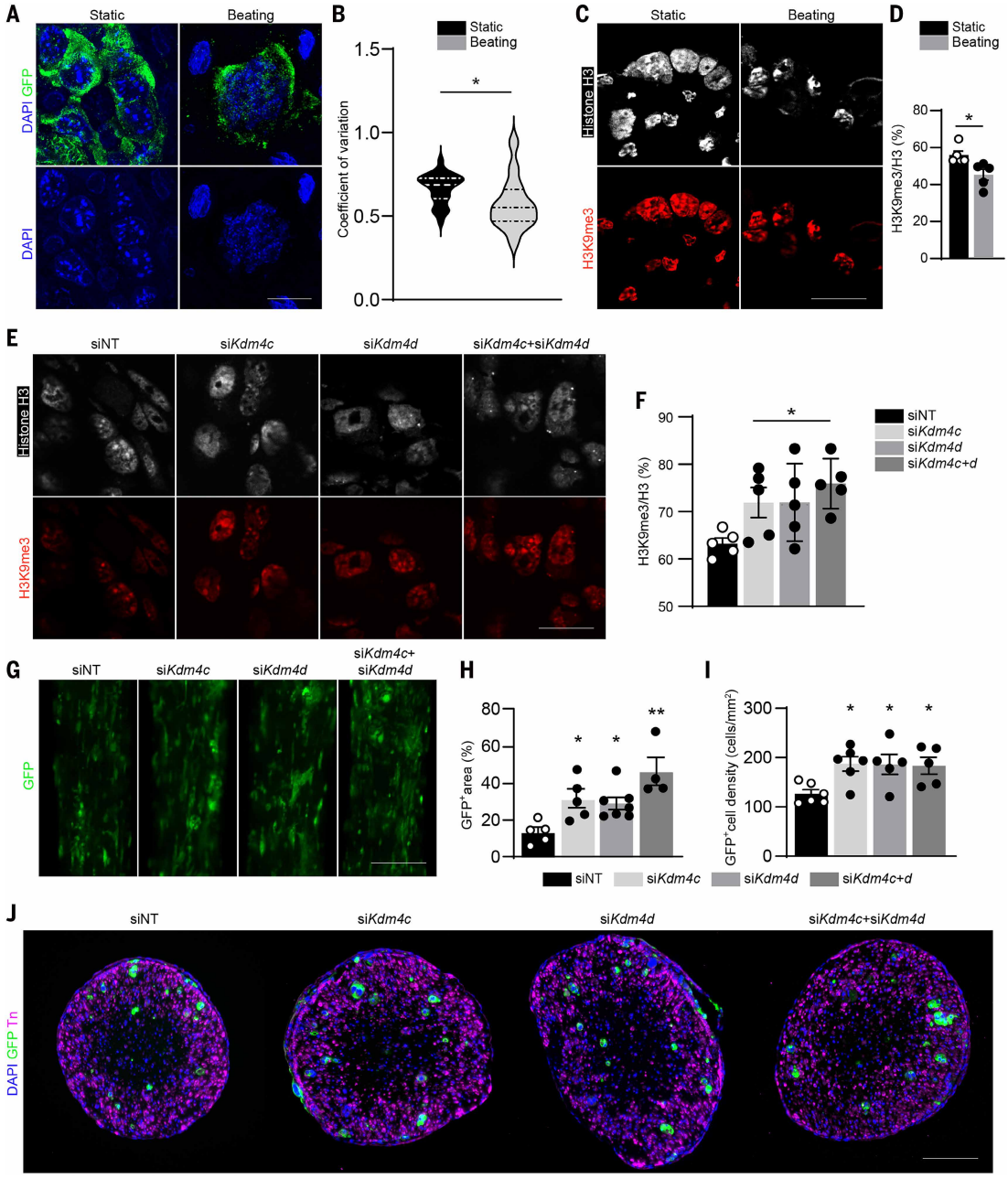

Fig. 5. Mechanical load reduces chromatin compaction and H3K9me3 in EHTs. (**A** and **B**) Representative images (A) and quantification (B) of chromatin compaction by DAPI staining of LG1233 GFP$^+$ cancer cells in static and beating EHTs ($n = 15$ to 25 nuclei from five beating and three static EHTs). (**C** and **D**) Representative images (C) and quantification (D) of colocalization of H3K9me3 with H3K9 in LG1233 GFP$^+$ cancer cells in static and beating EHTs ($n = 3$ to 5 biological replicates). (**E** and **F**) Representative images (E) and quantification (F) of colocalization of H3K9me3 with H3 in LG1233 GFP$^+$ cancer cells treated with the indicated siRNAs in beating EHTs ($n = 5$ biological replicates). (**G**) Representative low-magnification images of EHTs containing LG1233 GFP$^+$ cancer cells treated with the indicated siRNAs. (**H**) Quantification of the area occupied by LG1233 GFP$^+$ cancer cells upon treatment with the indicated siRNAs ($n = 4$ to 7 biological replicates). (**I**) Quantification of the density of LG1233 GFP$^+$ cancer cells in EHT cross sections upon treatment with the indicated siRNAs ($n = 5$ to 6 biological replicates). (**J**) Representative cross sections of EHTs containing LG1233 GFP$^+$ cancer cells treated with the indicated siRNAs. Scale bars: 10 μm (A); 20 μm [(C) and (E)]; 200 μm (G); 100 μm (J). Results were analyzed by either a two-tailed *t* test [(B) and (D)] or one-way ANOVA followed by a Dunnett's post hoc test [(F), (H), and (I)]. *$P < 0.05$; **$P < 0.01$. Data are mean ± SD.

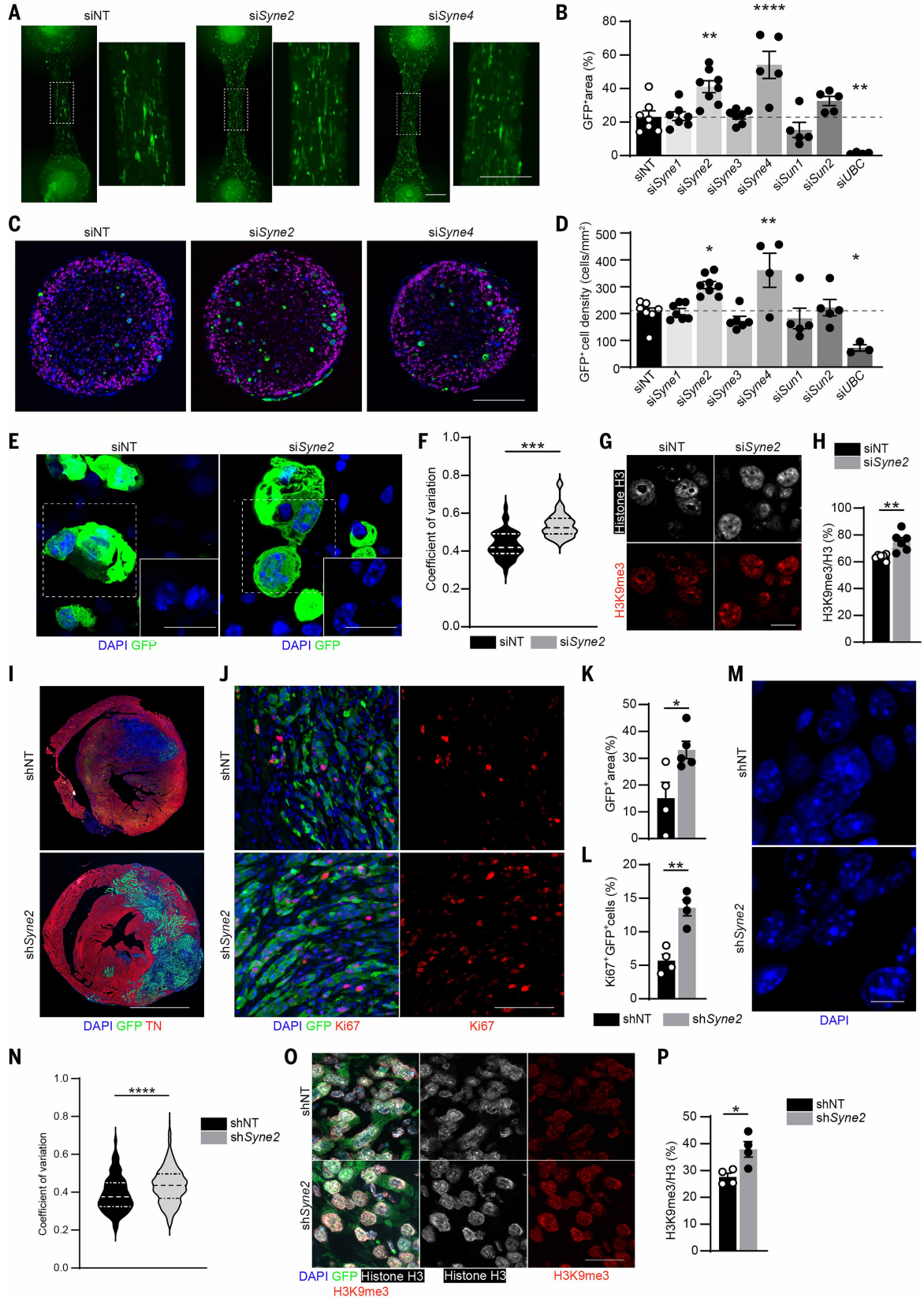

Fig. 6. Nesprin-2 is required by cancer cells to sense mechanical load and inhibit proliferation. (**A**) Representative images of EHTs containing GFP$^+$ LG1233 cells treated with the indicated siRNAs. A higher magnification of the squared region is shown on the right for each EHT. (**B**) Quantification of the area occupied by GFP$^+$ LG1233 cells treated with the indicated siRNAs ($n = 5$ to 8 biological replicates). (**C**) Cross sections of EHTs containing GFP$^+$ LG1233 cells treated with the indicated siRNAs. (**D**) Quantification of the GFP$^+$ LG1233 cell density in EHT cross sections upon treatment with the indicated siRNAs ($n = 3$ to 8 biological replicates). (**E**) Representative images of chromatin compaction by DAPI staining of GFP$^+$ LG1233 cells treated with indicated siRNA in EHTs. (**F**) Coefficient of variation calculated based on DAPI ($n = 43$ to 49 nuclei from seven siNTs and eight

si*Syne2*s). (**G** and **H**) Representative images (G) and quantification (H) of H3K9me3 and H3 colocalization in GFP$^+$ LG1233 cells treated with the indicated siRNAs in EHTs ($n = 6$ biological replicates). (**I**) Representative immunofluorescence images of hearts injected with GFP$^+$ LG1233 cells transduced with lentiviral vectors expressing the indicated shRNAs. CMs were stained for Tn. (**J**) High-magnification images of GFP$^+$ LG1233 cells transduced with the indicated shRNAs and injected into the heart, stained for Ki67. (**K**) Quantification of the area occupied by GFP$^+$ LG1233 cells transduced with the indicated shRNAs and injected into the heart ($n = 4$ to 5 biological replicates). (**L**) Quantification of GFP$^+$Ki67$^+$ LG1233 cells transduced with the indicated shRNAs and injected into the heart ($n = 4$ biological replicates). (**M** and **N**) Representative images (M) and coefficients of variation (N) of chromatin compaction by DAPI staining of GFP$^+$ LG1233 cells transduced with the indicated shRNAs ($n = 320$ to 400 nuclei from four hearts per group). (**O** and **P**) Representative images (O) and quantification (P) of H3K9me3 colocalization with total H3 in the nucleus of GFP$^+$ LG1233 cells transduced with the indicated shRNAs and injected into the heart ($n = 4$ biological replicates). Scale bars: 300 μm (A); 100 μm (C); 20 μm [(E) and (M)]; 10 μm (G); 3 mm (I); 50 μm (J); 30 μm (O). Results were analyzed by one-way ANOVA followed by a Dunnett's post hoc test [(B) and (D)] or a two-tailed *t* test [(F), (H), (K), (L), (N), and (P)]. $^*P < 0.05$; $^{**}P < 0.01$; $^{***}P < 0.001$; $^{****}P < 0.0001$. Data are mean ± SD.

tissue. In particular, mechanical load inhibited cell proliferation in both beating hearts in vivo and in EHTs in vitro, whereas unloading resulted in the opposite effect and restores cancer cell proliferative potential. The use of multiple and complementary models adds reliability to our findings, overcoming some limitations associated with both the HHT model (nonmechanical effects due to an inflammatory foreign-body response, which could alter the immune response to cancer cells) and the intracardiac injection of cancer cells (myocardial damage and repair processes that could affect cancer cell growth).

The effect of mechanical load on CM proliferation was already documented in humans implanted with LVAD and in a model of myocardial infarction in mice, showing that unloading promotes CM proliferation (*11*, *23*). Our findings provide evidence that a similar mechanism halts cancer cell proliferation in the heart, possibly protecting it from cancer. We initially focused on intracardiac implantation of lung adenocarcinoma cells, as the lung is constantly exposed to mechanical stimulation, similar to the heart. However, the type of mechanical force exerted on cancer cells that reside in the two organs is likely different. Whereas a compressive, positive pressure is exerted in the heart because of CM contraction, as also shown in our model, the lung is stretched by a negative pressure, exerted by diaphragm and intercostal muscle contraction. In addition, lung cancer is positioned in the middle of the list of cancer types that are reported to metastasize to the heart (*3*); thus, it appeared suitable to assess the effects of both increasing and decreasing mechanical load. We validated our findings using both melanoma and colon cancer cells, which disseminate to the heart at high and low frequency, respectively (*3*–*5*). We also used a genetic model in which cancer formation is induced by two oncogenic events that frequently occur in human cancers, namely, loss of p53 and expression of a mutated form of K-Ras. Using this model, we confirmed that the heart is protected from cancer, as activation of these two oncogenic events never resulted in aberrant cell proliferation in the heart, although it led to the formation of multiple rhabdomyosarcomas in peripheral muscles, similar to lesions induced in *LSL-K-Ras^{G12D};p53$^{f/+}$;MyoD-Cre* mice in which the Cre recombinase is expressed under the control of the *MyoD* muscle-specific promoter (*24*).

Mechanobiology has so far focused mainly on the mechanisms by which cells sense alterations in matrix stiffness and other physical properties of the extracellular milieu to eventually translate them into altered cell behaviors, such as proliferation and invasiveness (*25*, *26*). More limited information is available on the role of physical forces in modulating cell biology. Although several studies have analyzed the effects of cell stretch on gene expression and cell proliferation (*27*, *28*), our work provides evidence for the role of compressive forces, such as those generated in a beating heart, in inhibiting cancer cell growth. In line with our findings, cancer-associated fibroblasts have been reported to compress cancer cells, resulting in altered localization of YAP and decreased proliferation (*29*). Volumetric compression by osmotic pressure similarly inhibited melanoma cell proliferation and migration in culture (*30*).

We also explored whether alterations in cancer cell proliferation in the heart may be justified by metabolic competition for nutrients with beating CMs, which consume high amounts of energy. Our experimental data do not support this hypothesis, in line with the different metabolic substrates preferentially used by CMs (fatty acids) and cancer cells (glucose). In addition, cardiac unloading has been shown to shift CM metabolism toward glycolysis (*31*), which should further increase the competition and thus reduce cancer cell proliferation, which is exactly the opposite of what we observed. Still, we cannot exclude that other mechanisms different from mechanical stimulation could contribute to protect the heart from cancer.

To shed light on the mechanism that translates mechanical load into an inhibition of cell proliferation, we interrogated the transcriptome of cancer cells that reached and proliferated in the heart, as in the case of human cardiac metastases, and compared it with that of primary tumors and extracardiac metastases in the same individuals. Among the most up-regulated genes in cardiac metastases, independent of the tumor origin, were histone demethylases.

Aberrant histone modifications, including methylation at specific lysines, are among epigenetic alterations known to drive tumorigenesis (*32*–*35*). KDM proteins, which dynamically regulate histone methylation, have been associated with several aspects of cancer progression, including proliferation, migration, invasiveness, and drug resistance (*36*). There are eight KDM subfamilies (KDM1 to KDM8), differing in both structure and lysine targets (*36*). Both KDMs and histone lysine methyltransferases (KMTs) control cancer cell viability and tumor progression (*37*), implying a complex scenario in which chromatin organization influences multiple aspects of tumor growth. We focused on H3K9me3, as this is one of the major hallmarks of heterochromatin that promotes dynamic gene expression patterns, facilitating tumor evolution and aggressiveness in various cancers (*38*–*42*). In accordance with previous evidence showing that mechanical forces reduce H3K9me3 levels and the essential role of H3K9me3 in promoting chromatin compaction (*27*, *28*, *39*, *43*–*45*), our data indicate that mechanical load exerted by beating heart tissue reduces both H3K9me3 and chromatin compaction in cancer cells. Indeed, we invariably detected lower H3K9me3 levels and less-compact chromatin whenever mechanical load was increased in our experimental settings (in native versus heterotransplanted hearts in vivo, in overloaded versus unloaded EHTs, and in human cardiac metastases versus extracardiac lesions from the same patients). To assess whether these changes in H3K9me3 were causally associated with reduced cancer cell proliferation in response to mechanical load, we silenced KDM4C and KDM4D in cancer cells and showed that this indeed resulted in increased cell proliferation. These data are relevant considering recent clinical trials targeting both KDMs and KMTs for cancer therapy (*46*). Whether these treatments may have an impact on the incidence of cardiac cancers, as suggested by our findings, remains an open question and warrants further investigation.

Epigenetic modifications, such as H3K9me3, profoundly alter chromatin accessibility (*47*). By leveraging single-cell ATAC-seq (scATAC-seq) and H3K9me3 ChIP-seq on cancer cells injected in both loaded and unloaded hearts, we confirmed that mechanical load reduces H3K9me3 and increases chromatin accessibility for genes involved in cell cycle arrest, extracellular sensing, mechanosensing, cytoskeleton, and calcium homeostasis, consistent with reduced cancer cell growth. Among the up-regulated pathways, "maintenance of cell number" and "negative regulation of cell cycle" are obviously related to the reduced cancer cell proliferation observed in loaded hearts. Other up-regulated

pathways in both scATAC-seq and H3K9me3 ChIP-seq suggest that cancer cells respond to cardiac load by increasing their awareness of the extracellular space and stimuli by up-regulating mechanosensing pathways, such as "detection of abiotic stimulus," "detection of external stimulus," "response to mechanical stimulus," "mechanoreceptor differentiation," and "Notch signaling pathway." In addition, the up-regulation of several cytoskeleton-related pathways ("microtubule polymerization or depolymerization," "actomyosin structure organization," "positive regulation of cytoskeleton organization," and "actin filament organization") suggests that cancer cells reshape their structure to adapt to compressive forces in the beating heart. Lastly, our data indicate that cardiac load activates pathways involved in "regulation of lipid metabolic process," "regulation of carbohydrate metabolic process," and "glutathione metabolic process," which are notably altered in cancer (*48*, *49*), and in line with the evidence that mechanical cues influence cancer metabolism in different ways (*25*, *50*). Additionally, interesting pathways up-regulated in cancer cells growing in loaded hearts are those related to "calcium homeostasis," consistent with the evidence that loss of calcium homeostasis is an important driving force in the initiation and progression of malignant diseases (*51*).

Alterations in chromatin remodeling in response to extracellular stimuli usually involve the activity of members of the LINC complex, which is emerging as the most relevant mediator in mechanotransduction processes. Thus, we expected it to be part of the mechanosensing pathway used by cancer cells to respond to mechanical load in the heart, in line with several mutations in LINC complex–encoding genes that are associated with cardiomyopathies (*52*). Among its members, Nesprin-2 was identified as a key molecule required by multiple cancer cell types to halt their proliferation in response to mechanical load, as its silencing allowed cells to grow in both beating EHTs and hearts in vivo. Our data are consistent with the documented role of Nesprin-2 in regulating nuclear architecture, chromatin organization, and transcription of cancer-associated genes in response to adhesion forces (*53*). Conditional knockout of Nesprin-1 and Nesprin-2 in mice results in aberrant apoptosis, cardiac remodeling, fibrosis, and eventually heart failure, indicating that their role in mechanotransduction in the heart may be conserved across other cell types beyond cancer cells (*54*). Another study found that deletion of Nesprin-2 had little effect on cardiac function, although a 100 kDa Nesprin-2 isoform was still detected in mutant mice (*55*).

Collectively, the data presented in this work provide evidence that mechanical load in the heart inhibits cancer cell proliferation, likely explaining the low incidence of cardiac tumors. They also dig into the mechanisms responsible for this mechanoresponse, which involve Nesprin-2, histone methylation, and chromatin compaction. This offers fundamental insights into the biology of cell proliferation within the myocardium, and additionally, the mechanical stimuli that operate in a beating heart could be exploited for the development of a mechanical therapy for cancer.

Materials and methods

Animals

Animal experiments were conducted in accordance with guidelines from the Directive 2010/63/EU of the European Parliament on animal experimentation in compliance with European guidelines and International Laws and Policies (EC Council Directive 86/609, OJL 34, 12 December 1987) and were approved by the ICGEB Animal Welfare Board, the Ethical Committee, by the Austrian Ministry of Education, Science, and Culture (BMWFW-66.011/0155-WF/V/3b/2017) and by the Italian Ministry of Health (39/2025-D441B.69). Animals were housed in ventilated cages and subjected to a 12/12h light/dark cycle. Temperature was kept at 20° to 22°C and relative humidity at 45–65%. Animals of both sexes were used and randomly assigned to the different experimental groups.

Genetic model of primary cancer

LSL-K-Ras$^{G12D/+}$;p53$^{f/f}$ mice were used to induce oncogenic events by Adeno-Associated Virus 9 (AAV9) expressing the Cre recombinase (*56*). In this model, Cre drives both the expression of the endogenous *K-RasG12D* mutant oncogene and the homozygous deletion of wild-type *p53* tumor suppressor gene (*57*). Seven mice were intravenously injected with AAV9-Cre at the dose of 2 × 1012 vg/mouse. Animals were monitored for 2 months, and multiple organs were harvested for histological and *p53* recombination analysis.

Polymerase chain reacton–based detection of p53 recombination in LSL-K-RasG12D/+;p53f/f mice

Genomic DNA was isolated from frozen tissues (liver, heart, and skeletal muscle) of *LSL-K-Ras$^{G12D/+}$;p53$^{f/f}$* mice intravenously injected with AAV9-Cre, as well as from wild-type mice. Polymerase chain reaction (PCR) was performed using the Expand Long Template PCR System (Roche 11681834001). Specific primers against the *Trp53* gene (Fw: GGT TAA ACC CAG CTT GAC CA; Rev: GAG TCA GGC CCC ACT TTC TTG) were used to amplify both unrecombined (8800 bp) and recombined (700 bp) PCR products. Since the LG1233 cell line was generated upon Cre-recombination in *LSL-K-Ras$^{G12D/+}$;p53$^{f/f}$* mice (*16*), its genomic DNA was used as a positive control for the recombined PCR product. PCR products were separated on a 1% agarose gel, stained with Midori Green Advance (Nippon Genetics Europe MG04) and visualized using a Bio-Rad ChemiDoc Touch Imaging System.

Cancer cell lines

CT26-Cas9-hyg (GeneCopoeia, SL582) and LG1233 cells (kindly provided by F. Benvenuti) were cultured in DMEM medium (Thermo Fisher 10564011), supplemented with 10% Foetal Bovine Serum (FBS, Thermo Fisher A5256701) and 1% penicillin/streptomycin (Thermo Fisher 15140-122). Green Fluorescent B16-F10 cells (Innoprot/Innovative technologies in biological systems, P20121) were cultured in RPMI 1640 (Thermo Fisher 11875093), supplemented with 10% Foetal Bovine Serum (FBS, Thermo Fisher A5256701) and 1% penicillin/streptomycin (Thermo Fisher 15140-122).

Heterotopic heart transplantation

Heterotopic heart transplantation was performed using a modified cuff technique, in which the vessel wall is everted over a synthetic cylinder (*14*, *15*). Both donor and recipient mice were anesthetized with an intraperitoneal injection of xylazine (5 mg/kg) and ketamine (100 mg/kg). Donor mice were injected with heparin (50 IU, diluted in 0.4 ml saline solution) into the inferior vena cava for anticoagulation and the chest was open to expose the heart. The ascending aorta was cannulated with a 27G syringe at the level of the brachiocephalic trunk and perfused with cardioplegic solution at 4°C. The inferior and superior venae cava, as well as the pulmonary veins were ligated with 8-0 silk and transected distally to the ligatures. The heart was removed and kept in cardioplegic solution until implantation. In the meantime, cuffs for anastomoses were prepared, each one consisting of a cylindrical body and an extension for the placement of the vascular clamp. The cervical area of the recipient animal was opened, and the external jugular vein was divided between ligatures, to pull it through the cuff and occlude it proximally with a clamp. Upon removal of the ligature, the vessel wall was everted over the cuff and ligated with an 8-0 silk wire. The same procedure was applied to the common carotid artery. The cardiac graft was placed in the cervical region upside down to join the pulmonary trunk of the graft with the vein cuff construct of the recipient and the aorta of the graft with the everted artery of the recipient. Anastomoses were secured with circumferential 8-0 silk ligatures and clamps on the external jugular vein and carotid artery were removed sequentially. Mice were kept under a heat lamp until awake and carprofen (4 mg/kg every) and buprenorphine (0.1 mg/kg) were administered subcutaneously every 12 hours for 3 days to minimize pain. LG1233 cells (1 × 105 per animal) were injected into the left ventricle of either transplanted or native hearts (*8*). To label proliferating cells, 5-ethynyl-2′-deoxyuridine (EdU) (Thermo Fisher E10187) was

administered intraperitoneally on days 14, 18, 20 and 24 after LG1233 cell implantation. Animals were euthanized on day 28.

scATAC-seq

Heart samples were snap frozen in liquid nitrogen and sent to Active Motif for single nuclei preparation, Tn5 tagmentation, mRNA barcoding, NGS and bioinformatic analysis. Raw sequencing reads were processed using Cell Ranger ATAC with default parameters to perform read alignment and peak calling. For each sample, Signac (*58*) objects were generated and cellular barcodes were filtered based on quality control thresholds, requiring >10% of fragments in peaks, <10% of reads in ENCODE blacklist regions, transcription start site (TSS) enrichment >2, and nucleosome signal <4. High-quality samples were then merged for joint analysis with or without batch correction, followed by integration through a unified peak set, anchor identification, and dataset alignment. Dimensionality reduction was performed using term frequency–inverse document frequency transformation and singular value decomposition, with clustering based on a nearest-neighbor graph and visualization through uniform manifold approximation and projection at a default resolution of 0.2. Gene activity scores were computed from promoter (±2 kb) and gene-body accessibility, normalized with the "LogNormalize" method.

To identify modulated pathways in each cell type across conditions, we first performed differential analysis by the DamiRseq (*59*) (filtering low expressed genes) and LIMMA (*60*) (statistical analysis) R packages and, then, applied the gene set enrichment analysis (GSEA), using WEB-based GEne SeT AnaLysis Toolkit (WebGestalt) web tool (*61*) to analyze and annotate functional enrichment results. Data are archived in Zenodo (*62*).

ChIP-seq

Cancer cells were extracted from hearts and fixed in 1% PFA for 10 min. The fixation reaction was quenched with glycine at a final concentration of 125 mM and cells were sorted for GFP using FACS ARIA (BD). 1×10^6 cell pellets were snap-frozen and stored at -80°C until sonication.

Thawed pellets were lysed in SDS Buffer (50 mM Tris–HCl at pH 8.0, 5 mM EDTA at pH 8.0, 0.5% SDS and protease inhibitors Complete, Mini, Roche) and rocked 10 min at RT. Chromatin lysates were moved to 1.5 ml Bioruptor Microtubes and sonicated with a Bioruptor Pico sonicator.

Sonicated chromatin was diluted 3:2 (v/v) with Triton Dilution Buffer (100 mM Tris–HCl at pH 8.0, 250 mM NaCl, 5 mM EDTA at pH 8.0, 5% Triton X-100 and protease inhibitors) before immunoprecipitation with 3 µg of H3K9me3 antibody (Abcam ab176916).

Immunoprecipitation, washes and library preparation steps were done as reported (*63*), with minor changes. For the immunoprecipitation step, 25 µL/sample of magnetic Protein A beads (Dynabeads, Invitrogen) were used for capturing the antibody-chromatin complexes.

Sequencing of the ChIP-seq libraries was performed on a NovaSeq 6000 platform, generating 61 bp paired-end reads. Raw sequence data were processed with the nf-core/chipseq pipeline (v2.1.0) (10.5281/zenodo.3240506) with default parameters (*64*). Reads were aligned to the GRCm39 reference genome with BWA-MEM (v0.7.18) (*65*). Peaks enriched over input were called using the MACS3 broad peaks algorithm (v3.0.1) (*66*).

Differential binding analysis was performed using DiffBind (v3.16.0) (https://bioconductor.org/packages/release/bioc/vignettes/DiffBind/inst/doc/DiffBind.pdf) (*67*). Read counting was performed with the dba.count function, applying the parameter summits = FALSE to quantify enrichment across the full width of the called peaks. Differential analysis was executed with the default DESeq2 method. Differentially bound sites were defined by FDR<0.05. Finally, the results of the differential peak analysis were visualized using Circos (v0.69.9) (*68*). Enrichment Analysis has been performed using WEB-based GEne SeT AnaLysis Toolkit (WebGestalt) web tool (*61*) to identify Gene-Ontology Biological Processes (GO-BP) significantly dysregulated in loaded compared to unloaded conditions. Data are archived in Zenodo (*69*).

Generation of fibrin-based EHTs with adjustable mechanical load

CMs from neonatal Wistar rats (postnatal day 0-3) were harvested using Neonatal Cardiomyocyte dissociation kit (Miltenyi 130-098-373). Casting molds were prepared by inserting Teflon spacers (12 × 3 x 4 mm) inside a 24-well plate filled with 2% agarose (Invitrogen 15510-027) (*70*). After agarose jellification, the spacers were removed and a pair of silicone posts was placed in each well, with a 30G needle (Mesorelle) on the side of each post. The needle was bent to form a hook, close to the anchoring area of the silicone post.

To generate EHTs, 100 µL of reconstitution mixture, composed of 6×10^6 CMs/EHT, 5 mg/ml bovine fibrinogen (Sigma F8630), 20% DMEM 10x (Fisher scientific, 10134902), 10% heat inactivated horse serum (Thermo Fisher 26050-088) and 1% penicillin/streptomycin (Thermo Fisher 15140-122), was mixed with 3 µL thrombin (100 U/ml, Merck T7513) and pipetted into the casting molds containing silicon posts. EHT containing cancer cells were generated by adding cancer cells to the reconstitution mixture at the concentration of 2×10^4 LG1233 cells/EHT, 2×10^4 B16 cells/EHT and 3×10^4 CT26 cells/EHT, respectively. EHTs were placed in a humidified incubator at 37°C, 7% CO_2 for 2 hours to allow fibrinogen polymerization, and eventually transferred to new 24-well cell culture dishes. Medium, composed of DMEM (Biochrom F0415), 10% horse serum (Thermo Fisher 26050-088), 1% penicillin/streptomycin (Thermo Fisher 15140-122), insulin (10 µg/ml, Sigma-Aldrich I9278), and aprotinin (33 µg/ml, Merck A1153), was changed every other day. EHTs were monitored daily and considered mature upon appearance of coherent beating, between days 7 and 10 post casting (*17*). During the maturation period, hooks were not in contact with silicon posts, to not interfere with the spontaneous reduction of EHT length during maturation.

For load modulation, the system allowed for three distinct positions: a standard load position, achieved by the resistance offered by the silicone posts; an unload position, where the convex side of the hooks of the metal braces was rotated against the posts, reducing the distance between the two extremities of the EHTs; and an increased load position, where the concave side of the hook was rotated around the post, increasing the stiffness of the silicon posts and thus the mechanical load. To evaluate CM and cancer cell proliferation, EHTs were subjected to an EdU pulse matching the unload/increased load duration (72 hours). As an alternative method of unloading, EHTs were cultured in DMEM calcium-free (Thermo Fisher 21068028) for 5 days.

Cancer cell transfection and lentiviral transduction

Specific siRNAs (Horizon siGENOME SMARTpools, four siRNAs per target) targeting *UBC* (M-019408-01-0010), Non-Targeting Control siRNA # 4 (D-001210-04-20), *Kdm4c* (M-051504-00-0005), *Kdm4d* (M-052542-01-0005), *Syne1* (M-062644-00-0005), *Syne2* (M-056764-02-0005), *Syne3* (M-052180-01-0005), *Syne4* (M-054687-01-0005), *Sun1* (M-040715-00-0005), and *Sun2* (M-041247-01-0005) were diluted in Opti-MEM (Life Technologies 31985-047) and dispensed in 96-well or 6-well plates to a 50 nM final siRNA concentration. Lipofectamine RNAiMAX reagent (Invitrogen 13778-150) was diluted in Opti-MEM and added to the siRNA. After 30 min, cancer cells (LG1233, B16, CT26) were seeded on top of the siRNAs at a concentration of 1.5×10^4/cm2. For 2D culture, the medium was changed the day after transfection and cells were fixed after 5 days. For EHTs, cells were harvested the day after transfection and immediately added to EHT casting mixture.

To achieve a stable down-regulation of *Syne2,* cancer cells were transduced with lentiviral vectors containing either a short hairpin RNA (shRNA) targeting *Syne2* (Origene TL517485V) or a scramble shRNA control (Origene TR30021V) at MOI 1. After 48 hours, transduced cells were selected by adding 1 µg/ml of puromycin in the medium for 72 hours.

Real-time PCR

Cancer cells, either transfected with siRNA or transduced with viral vectors, were collected, centrifuged at 300 rcf for 5 min at 4°C, and

resuspended in TRIzol (Thermo Fisher, 15596026) for mRNA extraction and reverse transcription (1 μg) using the First Strand cDNA Synthesis Kit (Thermo Fisher, K1612). Target gene expression was evaluated using the GoTaq qPCR Master Mix Kit (Promega, A6002) on a CFX96 Real-Time System (Bio-Rad) with primers, reported in table S2. Expression of the mutated mRNA for K-RAS^{G12D} protein was detected using TaqPath ProAmp Master Mix (Thermo Fisher, A2094) and a custom TaqMan probe and primers (Thermo Fisher), reported in table S2.

Western blot

Cancer cells, either transfected with siRNA or transduced with viral vectors, were collected, centrifuged at 300 rcf for 5 min at 4°C, and resuspended in lysis buffer (100 mM Tris pH 7.4, 150 mM NaCl, 1 mM EDTA, 1% Triton X-100, 0.5% sodium deoxycholate). Lysates were sonicated and spun down at 14.000 rcf at 4°C for 10 min to remove debris. Protein lysates were separated in 5-8% polyacrylamide gel containing Protogel (PolyMed, EC890), 357 mM Bis-Tris HCl pH 6.8, APS (Sigma, 248614) and TEMED (Sigma, T7024). Proteins were transferred to a nitrocellulose membrane (Thermo Fisher, PB3210) using Power Blotter System (Thermo Fisher). Membranes were blocked in 5% non-fat milk in 0.1% Tween20 (Sigma, P9416) PBS (PBS-T) for 30 min at room temperature and incubated overnight at 4°C with primary antibodies against Nesprin-2 (GeneTex, GTX121928) and Nesprin-4 (Novus Biological, NBP1-59767), diluted 1:1000 and 1:500, respectively, in blocking solution. Membranes were incubated one hour at room temperature with HRP-conjugated secondary antibodies (Agilent, P044901-2), diluted 1:5000 in 5% bovine serum albumin (Sigma, A2328) in PBST. Immunoblots were developed by exposing membranes with Aersham ECL Western Blotting Detection Reagent (GE Healthcare, RPN2106) to either a chemiluminescent film (Thermo Fisher, AB406750) in a dark room or to ChemiDoc Touch (BioRad). Protein expression was quantified by analyzing the images of immunoblots using ImageJ.

Heart and EHT simulation

A finite element model was first created to represent the cardiac mechanics of a rodent LV under normal and unloaded conditions. The geometry was idealized as a truncated prolate ellipsoid with a wall thickness of 1.5 mm, a short axis radius of 4 mm, and a long axis radius of 8 mm. Myofiber angles were assumed to rotate from −60 degrees to +60 degrees from the endocardium to epicardium, with sheet orientations orthogonal to fibers and a calculated gradient direction between the epicardium and endocardium. Systolic contraction was simulated on this geometry using a FEniCS-based solver for cardiac mechanics (*71*), using P2 finite elements for displacement. Boundary conditions were implemented as a Robin type condition at the epicardium, an imposed endocardial pressure, and by fixing motion on the basal plane in the longitudinal direction. Active contraction was modeled using an active strain formulation, where the deformation tensor is multiplicatively decomposed into an active and passive form, and contraction along the fiber direction was controlled using an activation parameter, γ. The material was modeled as a transversely isotropic, slightly compressible hyperelastic material (*72*). Material parameters and additional modelling details are archived in Zenodo (*73*). Simulations were performed for a control case of end systole (end-systolic pressure, ESP = 15 kPa) and an unloaded case where the cavity pressure was removed (ESP = 0 kPa). In each case, deviatoric Cauchy stresses were calculated throughout the mesh in the fiber, sheet, and sheet normal direction, and volume averaged over the entire geometry.

For model validation, ultrasound images and corresponding measured chamber volumes from a native and transplanted heart were used to create truncated prolate ellipsoid LV models that fit the contoured epicardium and endocardium profiles and match the measured end diastolic volume (EDV), using end-diastolic pressures (EDPs) reported in previous studies on unloaded hearts (*74*), namely 1.3 kPa for native and 1.0 kPa for transplanted hearts, respectively. The end-systolic state was simulated by ramping endocardial pressures to literature values (13.5 kPa and 8.0 kPa for native and transplanted hearts, respectively (*74*)), and active strain increased to reach the ESV measured by ultrasound imaging. In both cases, total Cauchy stresses at end systole were calculated throughout the mesh in the fiber, sheet, and sheet normal direction, and volume was averaged over the entire geometry.

An additional model was created to simulate the mechanics of EHTs under different load conditions. A cylindrical geometry, 4000 μm in length and 300 μm in radius was meshed, and cardiac fibers were assigned along the length of the cylinder. A Robin type boundary condition was imposed on both ends to represent pillar traction under load. The spring constant of the Robin condition was first chosen to match experimental measurements of length change during contraction (~15%). This control was compared to simulations where the load was increased or decreased during systole to represent the modulation of the pillars in the experimental protocols. The spring constant was increased by 10X to simulate stiffening of the pillars, which resulted in decreased systolic shortening to ~11%. To represent unloading, the constant was reduced by 10-fold, so that the EHT was able to shorten with almost no resistance (~20%). Again, deviatoric Cauchy stresses were calculated throughout the mesh and volume averaged over a 300 μm-long section of the cylinder.

Spatial transcriptomics

Spatial transcriptomics was performed on samples of human cancers, upon approval by the Ethical Committee of the University of Trieste and Centro Cardiologico Monzino. Tissue sections (5 μm) were cut from corresponding formalin-fixed paraffin-embedded blocks and mounted on Superfrost slides (Thermo Fisher). Transcriptome analysis was undertaken on the NanoString GeoMx Digital Spatial Profiling platform in Seattle WA (USA). Tissue sections were stained for cell-specific markers (Troponin I for CMs, pan-cytokeratin for lung and colorectal cancer cells, PMEL for melanoma cells) to select the ROIs for subsequent gene expression analysis. ROIs were chosen to contain at least 300 cells for every cell type. Areas containing fibrosis or necrosis were excluded. Raw data are archived in Zenodo (*75*).

Histology and immunostaining

Tissues and EHTs were fixed in 10% formalin in PBS, embedded in paraffin and sliced in 4 μm sections using a microtome (Leica). Paraffin was removed by heat (60°C for 1 hour) and xylene bath (2 × 30 min) followed by rehydration by increasing ethanol dilutions. For H&E staining, sections were washed with water, incubated with haematoxylin for 2 min, followed by eosin for 5 min, and eventually dehydrated in 95% and 100% ethanol. For EdU and immunostaining, antigen retrieval was performed by boiling sections in 10 mM Tris base, 1 mM EDTA and 0.05% Tween 20 at pH 9.0 for 20 min in a microwave. Sections were rinsed three times in water and permeabilized 20 min in 0.5% Triton X-100 in PBS. For EdU detection, the Click-IT EdU 647 Imaging kit (Thermo Fisher C10247) was used. For antibody detection, sections were incubated in blocking solution (10% horse serum, 0.25% Triton X-100 in PBS) for 30 min, and stained overnight at 4°C with the following primary antibodies diluted in blocking solution: anti-cardiac Troponin I (Abcam ab47003), anti-cardiac Troponin T (Abcam ab8295), anti-phospho-Histone H3 (Ser10) (Merck 06-570), anti-Ki67 (Abcam ab15580), anti-PCM1 (Merck HPA023374), anti-Histone H3K9me3 (Abcam ab176916), anti-Histone H3 (Cell signaling D1H2), anti-PMEL (Abcam ab137078), anti-Cleaved caspase 3 (Cell Signaling 9661s), anti-RIPK3/RIP3 (Novus Biologicals NBP1-772999), anti-Aurora Kinase B (Abcam ab2254). Detection of primary antibodies was performed with Alexa Fluor©-conjugated secondary antibodies (Thermo Fisher), antibody labeling kits (Proteintech) or HRP-conjugated secondary antibodies (Thermo Fhisher). Nuclei were counterstained with either 4′,6-diamidino-2-phenylindole (DAPI; Thermo Fisher 62247) or Hoechst 33342 (Thermo Fisher H3570), and slides were mounted with Fluoromount-G Mounting Medium (Thermo Fisher 00-4958-02). Cross-sectional area was analyzed on sections stained by immunohistochemistry using an anti-dystrophin antibody (Abcam ab15277), VECTASTAIN ABC Kit

(Vectorlabs PK-6100) and ImmPACT DAB (Vectorlabs SK-4105), with minimal cross-sectional area set at 40 μm^2 (*62*).

Image acquisition and analysis

Images were acquired using a Nikon Eclipse T1 microscope equipped with an Andor Neo sCMOS camera, a Zeiss Apotome 3 microscope, equipped with Zeiss Axiocam 807 mono, and a Zeiss SIM ELYRA 7 equipped with PCO.edge 4.2 sCMOS camera (Excelitas), and analyzed by ImageJ (NIH, Bethesda). DNA compaction was evaluated by the analysis of the CV (*76*). CV of individual nuclei was calculated as CV = σ/μ, where σ represents the standard deviation of the DAPI intensity values, and μ represents the mean value of intensity of the nucleus. In the highly condensed chromatin, bright chromocenters lead to a wider intensity distribution and, consequently, a higher standard deviation compared with decondensed heterochromatin, characterized by more uniform DAPI staining.

H3K9me3 quantification was performed by measuring pixel colocalization over total histone H3, using ImageJ. Number of proliferating cancer cells and cancer cell density in cross-sectional areas were calculated using the Cell Counter plugin of ImageJ.

EHT video optical recording and analysis

EHT contraction was recorded using a Nikon Eclipse T1 microscope equipped with Andor Neo sCMOS camera and a Plan UW 2X objective. EHTs were kept in a humidified incubator (OkoLab) at 37°C, 7% CO_2 during live imaging. Recording was performed for 5 s at 100 frames per second. For stimulated contraction measurements, EHTs were electrical stimulated at 4 Hz using a Hugo Sachs Elektronik Stimulator c type 224, as previously described (*17*).

Based on post geometry, the elastic modulus of Sylgard 184 (2.6 kPa) and the distance between the posts (post deflection), force was calculated according to a published equation (*77*). For a post of radius R and length L, cast from material with a known elastic modulus (E), the moment of inertia (I) is given by $I = 1/4R4$ and force based on post deflection δ by the formula:

$$F = 3\mathrm{EI}\delta / (L3) = (3\pi \mathrm{ER}4\delta) / (4L3) \quad (1)$$

Statistical analysis

The number of animals for each experimental procedure was determined using the GPower 3.1 software, considering a statistical power ($\prod$) of 80% and a probability of committing a Type I error (α) of 0.05. Results were expressed as mean ± standard error of the mean (SEM). Student's t test was used to compare two groups, one-way ANOVA followed by Bonferroni's multiple comparison was used to compare multiple sample groups with one control, ordinary one-way ANOVA followed by Dunnet multiple comparison was used to compare multiple measurements of distinct sample groups. All tests were performed using GraphPad Prism 6 (GraphPad Software, La Jolla California USA). Results with the following P values were considered statistically significant: $^{*}P \leq 0.05$; $^{**}P \leq 0.01$; $^{***}P \leq 0.001$.

REFERENCES AND NOTES

1. R. Gupta, V. Meghrajani, R. Desai, N. Gupta, Primary Malignant Cardiac Tumors: A Rare Disease With an Adventurous Journey. *J. Am. Heart Assoc.* **9**, e016032 (2020). doi: 10.1161/JAHA.120.016032; pmid: 32389052
2. I. Burazor *et al.*, Metastatic cardiac tumors: From clinical presentation through diagnosis to treatment. *BMC Cancer* **18**, 202 (2018). doi: 10.1186/s12885-018-4070-x; pmid: 29463229
3. R. Bussani, F. De-Giorgio, A. Abbate, F. Silvestri, Cardiac metastases. *J. Clin. Pathol.* **60**, 27–34 (2007). doi: 10.1136/jcp.2005.035105; pmid: 17098886
4. R. Bussani *et al.*, Cardiac Tumors: Diagnosis, Prognosis, and Treatment. *Curr. Cardiol. Rep.* **22**, 169 (2020). doi: 10.1007/s11886-020-01420-z; pmid: 33040219
5. L. M. Nova-Camacho *et al.*, Cardiac Metastasis From Solid Cancers: A 35-Year Single-Center Autopsy Study. *Arch. Pathol. Lab. Med.* **147**, 177–184 (2023). doi: 10.5858/arpa.2021-0418-OA; pmid: 35639589
6. M. Giacca, S. Zacchigna, Harnessing the microRNA pathway for cardiac regeneration. *J. Mol. Cell. Cardiol.* **89** (Pt A), 68–74 (2015). doi: 10.1016/j.yjmcc.2015.09.017; pmid: 26431632
7. S. Zacchigna, M. Giacca, Extra- and intracellular factors regulating cardiomyocyte proliferation in postnatal life. *Cardiovasc. Res.* **102**, 312–320 (2014). doi: 10.1093/cvr/cvu057; pmid: 24623280
8. T. Kocijan *et al.*, Genetic lineage tracing reveals poor angiogenic potential of cardiac endothelial cells. *Cardiovasc. Res.* **117**, 256–270 (2021). doi: 10.1093/cvr/cvaa012; pmid: 31999325
9. D. Sedmera *et al.*, Spatiotemporal pattern of commitment to slowed proliferation in the embryonic mouse heart indicates progressive differentiation of the cardiac conduction system. *Anat. Rec. A Discov. Mol. Cell. Evol. Biol.* **274**, 773–777 (2003). doi: 10.1002/ar.a.10085; pmid: 12923887
10. R. P. Thompson *et al.*, The oldest, toughest cells in the heart. *Novartis Found. Symp.* **250**, 157–174, discussion 174–176, 276–279 (2003). doi: 10.1002/0470868066.ch10; pmid: 12956329
11. D. C. Canseco *et al.*, Human ventricular unloading induces cardiomyocyte proliferation. *J. Am. Coll. Cardiol.* **65**, 892–900 (2015). doi: 10.1016/j.jacc.2014.12.027; pmid: 25618530
12. K. Reynen, U. Köckeritz, R. H. Strasser, Metastases to the heart. *Ann. Oncol.* **15**, 375–381 (2004). doi: 10.1093/annonc/mdh086; pmid: 14998838
13. S. Zacchigna, L. Zentilin, M. Giacca, Adeno-associated virus vectors as therapeutic and investigational tools in the cardiovascular system. *Circ. Res.* **114**, 1827–1846 (2014). doi: 10.1161/CIRCRESAHA.114.302331; pmid: 24855205
14. T. Ratschiller *et al.*, Heterotopic Cervical Heart Transplantation in Mice. *J. Vis. Exp.* **102**, e52907 (2015). pmid: 26325193
15. R. Oberhuber *et al.*, Murine cervical heart transplantation model using a modified cuff technique. *J. Vis. Exp.* **92**, e50753 (2014). pmid: 25350682
16. N. Dimitrova *et al.*, Stromal Expression of miR-143/145 Promotes Neoangiogenesis in Lung Cancer Development. *Cancer Discov.* **6**, 188–201 (2016). doi: 10.1158/2159-8290.CD-15-0854; pmid: 26586766
17. A. Hansen *et al.*, Development of a drug screening platform based on engineered heart tissue. *Circ. Res.* **107**, 35–44 (2010). doi: 10.1161/CIRCRESAHA.109.211458; pmid: 20448218
18. C. Dupont *et al.*, Evidence for low nanocompaction of heterochromatin in living embryonic stem cells. *EMBO J.* **42**, e110286 (2023). doi: 10.15252/embj.2021110286; pmid: 37082862
19. J. Ramírez-Cuéllar *et al.*, LATS1 controls CTCF chromatin occupancy and hormonal response of 3D-grown breast cancer cells. *EMBO J.* **43**, 1770–1798 (2024). doi: 10.1038/s44318-024-00080-x; pmid: 38565950
20. M. Salinas-Pena, E. Rebollo, A. Jordan, Imaging analysis of six human histone H1 variants reveals universal enrichment of H1.2, H1.3, and H1.5 at the nuclear periphery and nucleolar H1X presence. *eLife* **12**, 91306 (2024). doi: 10.7554/eLife.91306.3; pmid: 38530350
21. Z. H. Gray, M. A. Honer, P. Ghatalia, Y. Shi, J. R. Whetstine, 20 years of histone lysine demethylases: From discovery to the clinic and beyond. *Cell* **188**, 1747–1783 (2025). doi: 10.1016/j.cell.2025.02.023; pmid: 40185081
22. A. Méjat, T. Misteli, LINC complexes in health and disease. *Nucleus* **1**, 40–52 (2010). doi: 10.4161/nucl.1.1.10530; pmid: 21327104
23. R. Suzuki *et al.*, The reduction of hemodynamic loading assists self-regeneration of the injured heart by increasing cell proliferation, inhibiting cell apoptosis, and inducing stem-cell recruitment. *J. Thorac. Cardiovasc. Surg.* **133**, 1051–1058 (2007). doi: 10.1016/j.jtcvs.2006.12.026; pmid: 17382652
24. K. Nakahata *et al.*, K-Ras and p53 mouse model with molecular characteristics of human rhabdomyosarcoma and translational applications. *Dis. Model. Mech.* **15**, 049004 (2022). doi: 10.1242/dmm.049004; pmid: 35174853
25. R. Bertolio, F. Napoletano, G. Del Sal, Dynamic links between mechanical forces and metabolism shape the tumor milieu. *Curr. Opin. Cell Biol.* **84**, 102218 (2023). doi: 10.1016/j.ceb.2023.102218; pmid: 37597464
26. H. Mohammadi, E. Sahai, Mechanisms and impact of altered tumour mechanics. *Nat. Cell Biol.* **20**, 766–774 (2018). doi: 10.1038/s41556-018-0131-2; pmid: 29950570
27. H. Q. Le *et al.*, Mechanical regulation of transcription controls Polycomb-mediated gene silencing during lineage commitment. *Nat. Cell Biol.* **18**, 864–875 (2016). doi: 10.1038/ncb3387; pmid: 27398909
28. M. M. Nava *et al.*, Heterochromatin-Driven Nuclear Softening Protects the Genome against Mechanical Stress-Induced Damage. *Cell* **181**, 800–817.e22 (2020). doi: 10.1016/j.cell.2020.03.052; pmid: 32302590
29. J. Barbazan *et al.*, Cancer-associated fibroblasts actively compress cancer cells and modulate mechanotransduction. *Nat. Commun.* **14**, 6966 (2023). doi: 10.1038/s41467-023-42382-4; pmid: 37907483
30. X. Zhang *et al.*, Compression drives diverse transcriptomic and phenotypic adaptations in melanoma. *Proc. Natl. Acad. Sci. U.S.A.* **120**, e2220062120 (2023). doi: 10.1073/pnas.2220062120; pmid: 37722033
31. N. A. Diakos *et al.*, Evidence of Glycolysis Up-Regulation and Pyruvate Mitochondrial Oxidation Mismatch During Mechanical Unloading of the Failing Human Heart: Implications for Cardiac Reloading and Conditioning. *JACC Basic Transl. Sci.* **1**, 432–444 (2016). doi: 10.1016/j.jacbts.2016.06.009; pmid: 28497127
32. X. An, X. Lan, Z. Feng, X. Li, Q. Su, Histone modification: Biomarkers and potential therapies in colorectal cancer. *Ann. Hum. Genet.* **87**, 274–284 (2023). doi: 10.1111/ahg.12528; pmid: 37712180
33. J. E. Audia, R. M. Campbell, Histone Modifications and Cancer. *Cold Spring Harb. Perspect. Biol.* **8**, a019521 (2016). doi: 10.1101/cshperspect.a019521; pmid: 27037415
34. Y. Chen *et al.*, The role of histone methylation in the development of digestive cancers: A potential direction for cancer management. *Signal Transduct. Target. Ther.* **5**, 143 (2020). doi: 10.1038/s41392-020-00252-1; pmid: 32747629

35. J. Zhuang, Q. Huo, F. Yang, N. Xie, Perspectives on the Role of Histone Modification in Breast Cancer Progression and the Advanced Technological Tools to Study Epigenetic Determinants of Metastasis. *Front. Genet.* **11**, 603552 (2020). doi: 10.3389/fgene.2020.603552; pmid: 33193750
36. J. Sterling, S. V. Menezes, R. H. Abbassi, L. Munoz, Histone lysine demethylases and their functions in cancer. *Int. J. Cancer* **148**, 2375–2388 (2021). doi: 10.1002/ijc.33375; pmid: 33128779
37. J. C. Black, C. Van Rechem, J. R. Whetstine, Histone lysine methylation dynamics: Establishment, regulation, and biological impact. *Mol. Cell* **48**, 491–507 (2012). doi: 10.1016/j.molcel.2012.11.006; pmid: 23200123
38. Y. Yokoyama *et al.*, Cancer-associated upregulation of histone H3 lysine 9 trimethylation promotes cell motility in vitro and drives tumor formation in vivo. *Cancer Sci.* **104**, 889–895 (2013). doi: 10.1111/cas.12166; pmid: 23557258
39. V. Gaggioli *et al.*, Dynamic de novo heterochromatin assembly and disassembly at replication forks ensures fork stability. *Nat. Cell Biol.* **25**, 1017–1032 (2023). doi: 10.1038/s41556-023-01167-z; pmid: 37414849
40. A. Lam-Ubol, E. Phattarataratip, Distinct histone H3 modification profiles correlate with aggressive characteristics of salivary gland neoplasms. *Sci. Rep.* **12**, 15063 (2022). doi: 10.1038/s41598-022-19174-9; pmid: 36064736
41. E. Z. Keung *et al.*, Increased H3K9me3 drives dedifferentiated phenotype via KLF6 repression in liposarcoma. *J. Clin. Invest.* **125**, 2965–2978 (2015). doi: 10.1172/JCI77976; pmid: 26193637
42. M. W. Chen *et al.*, H3K9 histone methyltransferase G9a promotes lung cancer invasion and metastasis by silencing the cell adhesion molecule Ep-CAM. *Cancer Res.* **70**, 7830–7840 (2010). doi: 10.1158/0008-5472.CAN-10-0833; pmid: 20940408
43. D. Djeghloul *et al.*, Loss of H3K9 trimethylation alters chromosome compaction and transcription factor retention during mitosis. *Nat. Struct. Mol. Biol.* **30**, 489–501 (2023). doi: 10.1038/s41594-023-00943-7; pmid: 36941433
44. H. J. Bae *et al.*, Cyclic stretch induced epigenetic activation of periodontal ligament cells. *Mater. Today Bio* **26**, 101050 (2024). doi: 10.1016/j.mtbio.2024.101050; pmid: 38654935
45. J. Sun, J. Chen, E. Mohagheghian, N. Wang, Force-induced gene up-regulation does not follow the weak power law but depends on H3K9 demethylation. *Sci. Adv.* **6**, eaay9095 (2020). doi: 10.1126/sciadv.aay9095; pmid: 32270037
46. X. Yu *et al.*, Cancer epigenetics: From laboratory studies and clinical trials to precision medicine. *Cell Death Discov.* **10**, 28 (2024). doi: 10.1038/s41420-024-01803-z; pmid: 38225241
47. M. Ninova, K. Fejes Tóth, A. A. Aravin, The control of gene expression and cell identity by H3K9 trimethylation. *Development* **146**, dev181180 (2019). doi: 10.1242/dev.181180; pmid: 31540910
48. L. A. Broadfield, A. A. Pane, A. Talebi, J. V. Swinnen, S. M. Fendt, Lipid metabolism in cancer: New perspectives and emerging mechanisms. *Dev. Cell* **56**, 1363–1393 (2021). doi: 10.1016/j.devcel.2021.04.013; pmid: 33945792
49. L. Kennedy, J. K. Sandhu, M. E. Harper, M. Cuperlovic-Culf, Role of Glutathione in Cancer: From Mechanisms to Therapies. *Biomolecules* **10**, 1429 (2020). doi: 10.3390/biom10101429; pmid: 33050144
50. Y. Zhang *et al.*, Mechanical forces in the tumor microenvironment: Roles, pathways, and therapeutic approaches. *J. Transl. Med.* **23**, 313 (2025). doi: 10.1186/s12967-025-06306-8; pmid: 40075523
51. S. Zheng, X. Wang, D. Zhao, H. Liu, Y. Hu, Calcium homeostasis and cancer: Insights from endoplasmic reticulum-centered organelle communications. *Trends Cell Biol.* **33**, 312–323 (2023). doi: 10.1016/j.tcb.2022.07.004; pmid: 35915027
52. M. J. Stroud, Linker of nucleoskeleton and cytoskeleton complex proteins in cardiomyopathy. *Biophys. Rev.* **10**, 1033–1051 (2018). doi: 10.1007/s12551-018-0431-6; pmid: 29869195
53. F. Li Mow Chee *et al.*, Mena regulates nesprin-2 to control actin-nuclear lamina associations, trans-nuclear membrane signalling and gene expression. *Nat. Commun.* **14**, 1602 (2023). doi: 10.1038/s41467-023-37021-x; pmid: 36959177
54. I. Banerjee *et al.*, Targeted ablation of nesprin 1 and nesprin 2 from murine myocardium results in cardiomyopathy, altered nuclear morphology and inhibition of the biomechanical gene response. *PLOS Genet.* **10**, e1004114 (2014). doi: 10.1371/journal.pgen.1004114; pmid: 24586179
55. E. L. Leong *et al.*, Nesprin-1 LINC complexes recruit microtubule cytoskeleton proteins and drive pathology in Lmna-mutant striated muscle. *Hum. Mol. Genet.* **32**, 177–191 (2023). doi: 10.1093/hmg/ddac179; pmid: 35925868
56. I. Secco *et al.*, Genetic tracing and topography of spontaneous and stimulated cardiac regeneration in mice. *Nat. Cardiovasc. Res.* **4**, 397–411 (2025). doi: 10.1038/s44161-025-00623-3; pmid: 40055464
57. E. L. Jackson *et al.*, The differential effects of mutant p53 alleles on advanced murine lung cancer. *Cancer Res.* **65**, 10280–10288 (2005). doi: 10.1158/0008-5472.CAN-05-2193; pmid: 16288016
58. T. Stuart, A. Srivastava, S. Madad, C. A. Lareau, R. Satija, Single-cell chromatin state analysis with Signac. *Nat. Methods* **18**, 1333–1341 (2021). doi: 10.1038/s41592-021-01282-5; pmid: 34725479
59. M. Chiesa, G. I. Colombo, L. Piacentini, DaMiRseq-an R/Bioconductor package for data mining of RNA-Seq data: Normalization, feature selection and classification. *Bioinformatics* **34**, 1416–1418 (2018). doi: 10.1093/bioinformatics/btx795; pmid: 29236969
60. M. E. Ritchie *et al.*, limma powers differential expression analyses for RNA-sequencing and microarray studies. *Nucleic Acids Res.* **43**, e47 (2015). doi: 10.1093/nar/gkv007; pmid: 25605792
61. J. M. Elizarraras *et al.*, WebGestalt 2024: Faster gene set analysis and new support for metabolomics and multi-omics. *Nucleic Acids Res.* **52** (W1), W415–W421 (2024). doi: 10.1093/nar/gkae456; pmid: 38808672
62. M. Chiesa, S. Zacchigna, scATAC-seq for paper: "Mechanical load protects the heart from cancer," Zenodo (2026); https://doi.org/10.5281/zenodo.18393459.
63. G. I. Dellino *et al.*, Release of paused RNA polymerase II at specific loci favors DNA double-strand-break formation and promotes cancer translocations. *Nat. Genet.* **51**, 1011–1023 (2019). doi: 10.1038/s41588-019-0421-z; pmid: 31110352
64. P. A. Ewels *et al.*, The nf-core framework for community-curated bioinformatics pipelines. *Nat. Biotechnol.* **38**, 276–278 (2020). doi: 10.1038/s41587-020-0439-x; pmid: 32055031
65. H. Li, R. Durbin, Fast and accurate short read alignment with Burrows-Wheeler transform. *Bioinformatics* **25**, 1754–1760 (2009). doi: 10.1093/bioinformatics/btp324; pmid: 19451168
66. Y. Zhang *et al.*, Model-based analysis of ChIP-Seq (MACS). *Genome Biol.* **9**, R137 (2008). doi: 10.1186/gb-2008-9-9-r137; pmid: 18798982
67. C. S. Ross-Innes *et al.*, Differential oestrogen receptor binding is associated with clinical outcome in breast cancer. *Nature* **481**, 389–393 (2012). doi: 10.1038/nature10730; pmid: 22217937
68. M. Krzywinski *et al.*, Circos: An information aesthetic for comparative genomics. *Genome Res.* **19**, 1639–1645 (2009). doi: 10.1101/gr.092759.109; pmid: 19541911
69. L. Ciacci, G. I. Dellino, G. Pellicci, ChIP-Seq Dataset related to "Mechanical load protects the heart from cancer," Zenodo (2026); https://doi.org/10.5281/zenodo.18404913.
70. G. Ciucci *et al.*, Engineered heart tissue maturation inhibits cardiomyocyte proliferative response to cryoinjury. *J. Tissue Eng.* **14**, 20417314231190147 (2023). doi: 10.1177/20417314231190147; pmid: 37842206
71. H. N. T. Finsberg, pulse: A python package based on FEniCS for solving problems in cardiac mechanics. *J. Open Source Softw.* **4**, 1539 (2019). doi: 10.21105/joss.01539
72. G. A. Holzapfel, R. W. Ogden, Constitutive modelling of passive myocardium: A structurally based framework for material characterization. *Philos. Trans. A Math. Phys. Eng. Sci.* **367**, 3445–3475 (2009). doi: 10.1098/rsta.2009.0091; pmid: 19657007
73. S. Wall, ComputationalPhysiology/ciucci-2025: v2.0.0, Zenodo (2025); https://doi.org/10.5281/zenodo.17207215.
74. M. Didié *et al.*, Preservation of left ventricular function and morphology in volume-loaded versus volume-unloaded heterotopic heart transplants. *Am. J. Physiol. Heart Circ. Physiol.* **305**, H533–H541 (2013). doi: 10.1152/ajpheart.00218.2013; pmid: 23771692
75. M. Chiesa, D. Lorizio, S. Zacchigna, Dataset related to the article "Mechanical load protects the heart from cancer," Zenodo (2024); https://doi.org/10.5281/zenodo.13785810.
76. L. Martin *et al.*, A protocol to quantify chromatin compaction with confocal and super-resolution microscopy in cultured cells. *STAR Protoc.* **2**, 100865 (2021). doi: 10.1016/j.xpro.2021.100865; pmid: 34632419
77. H. Vandenburgh *et al.*, Drug-screening platform based on the contractility of tissue-engineered muscle. *Muscle Nerve* **37**, 438–447 (2008). doi: 10.1002/mus.20931; pmid: 18236465

ACKNOWLEDGMENTS

We are grateful to F. Benvenuti for sharing LG1233 cells and to B. Boziglav for excellent technical assistance. **Funding:** This work was supported by the project PROMOS, funded by the European Union under the Interreg VI-A Italy–Austria Programme 2021–2027 through the European Regional Development Fund; Worldwide Cancer Research under grant no. 24-0071; AIRC under grant IG 2020- ID 24529 project, P.I. S.Z.; FISA-2022-00721 CANCEL, Avviso FISA D.D. 1405 13/09/2022, funded by the Italian Ministry of University and Research (MUR) (CUP F93C24000140004); projects of the National Center for Gene Therapy and Drugs based on RNA Technology, within the National Recovery and Resilience Plan (PNRR) (CUP J93C22000530006); PRIN McHeart, funded by MUR (CUP J53D23012580006), to S.Z.; PNRR-TR1-2023-12378449 (CUP B43C24000350006), NRRP M6C2I2.1 – NextGenerationEU, to G.P.; DZHK (German Centre for Cardiovascular Research, FKZ 81Z0710115 and 81X2710153) and European Union's Horizon 2020 research and innovation program (874764) to T.E. **Author contributions:** S.Z. and F.S.L. conceived the idea of the work; G.C. performed most of the experiments; D.L., G.L.P., and M.C. performed spatial transcriptomics and analysis; N.B., S.B., and I.L.C.D.G. contributed to analyze EHT data; ; A.C. and E.Z. analyzed HHT data; S.W. and H.N.F performed heart and EHT simulation; M.B., S.V., B.T., A.-V.N., B.C., R.V., F.R., and R.O. performed in vivo experiments; L.C., G.I.D., and P.G.P. preformed ChIP-seq experiments; M.M., G.S., M.G., T.E., R.B., F.S., L.A., M.D.F., G.P., and P.G. provided critical insight and analyzed data; and S.Z., G.C., and A.C. wrote the manuscript. **Competing interests** : S.W. holds equity in Organos Inc, a cardiac drug discovery company that uses a stem cell–based technology similar to that described in the manuscript. **Data, code, and materials availability:** The data supporting the findings from this study are available within the manuscript and the supplementary materials. Data related to mathematical modeling (*73*), ATAC-seq (*62*), ChIP-seq (*69*), and spatial transcriptomics (*75*) are archived in Zenodo. Materials generated in this study will be made available upon request.

SUPPLEMENTARY MATERIALS

science.org/doi/10.1126/science.ads9412
Figs. S1 to S16; Tables S1 and S2; Reproducibility Checklist; Movies S1 and S2
Submitted 5 September 2024; resubmitted 17 October 2025; accepted 27 February 2026
10.1126/science.ads9412

Correction (19 May 2026): In Fig. 3A, the lung adenocarcinoma image for patient 1 was inadvertently duplicated and covered the adrenal and lung metastasis images for patient 3. The figure has been replaced.

Mechanical load inhibits cancer growth in mouse and human hearts

Giulio Ciucci, Daniela Lorizio, Nicoletta Bartoloni, Mauricio Budini, Andrea Colliva, Simone Vodret, Anh-Vu Nguyen, Lorenzo Ciacci, Bernhard Texler, Benno Cardini, Rupert Oberhuber, Sofia Bindelli, Ilaria Luciana Carlotta Del Giudice, Roman Vuerich, Francesco Riccitelli, Elena Zago, Henrik Nicolay Finsberg, Mattia Chiesa, Gianluca Lorenzo Perrucci, Rossana Bussani, Furio Silvestri, Manuel Maglione, Gaetano Ivan Dellino, Gianfranco Sinagra, Mauro Giacca, Thomas Eschenhagen, Paolo Golino, Giulio Pompilio, Pier Giuseppe Pelicci, Laura Andolfi, Maurizio Pinamonti, Matteo Dal Ferro, Samuel Wall, Francesco S. Loffredo, and Serena Zacchigna

Science **392** (6796), eads9412. DOI: 10.1126/science.ads9412

Editor's summary

It is very rare for cancer to either form in or metastasize to the heart, suggesting that there is something that inhibits cancer growth in the cardiac microenvironment. A key potential explanation is mechanical load. Ciucci *et al*. tested this idea by introducing cancer cells into rodent hearts and then in vitro engineering cardiac models with or without normal mechanical load. They also compared human tissue samples from rare cardiac metastases and corresponding extracardiac tumors. The authors determined that increased mechanical load promoted Nesprin-2 signaling, which then led to changes in chromatin compaction and histone methylation, resulting in the suppression of cancer growth (see the Perspective by Paltzer and Martin). —Yevgeniya Nusinovich